Imprint of Subluminal Gravitational Waves in PTA Data

Bachelor thesis
submitted to the

University of Münster
Institute für Theoretical Physics

by
Nina Cordes

August 2024

First examiner:	Jun.- Prof. Dr. Kai Schmitz
Second examiner:	Prof. Dr. Anna Kulesza
Day of submission:	Thursday 29th August, 2024

Abstract

Pulsar Timing Arrays (PTAs) are an important tool for the detection and study of gravitational waves (GWs) in the nanohertz frequency range. Pulsars, which are rotating neutron stars, emit signals in the form of pulses, which can be timed with high precision. The arrival times of these pulses are affected by perturbations in the space-time metric caused by passing GWs. The characteristic pattern of this effect is describe through the overlap reduction function (ORF) Γ_{ab}, which in general relativity (GR) is described by the Hellings and Downs (HD) curve. In this thesis, two established derivations of the HD curve are examined: an analytical approach and one using a decomposition into spherical harmonics. The analytical approach provides fundamental insights into the HD curve within the context of GR. The spherical harmonics method is employed to analyze corrections to the HD curve resulting from modified gravity theories, specifically for subluminal phase velocities. A discussion of the auto-correlation coefficient Γ_{aa} reveals that it does not diverge in modified gravity, as previously assumed, but can be expressed analytically. Previous work shows that a simplified ORF $\Gamma_{ab}^{\mathrm{SIM}}$ can be derived for sufficient small phase velocities $v_{ph} \ll 1$, resulting in a proportionality of the cross-power spectrum S_{ab} to $fL_aA^2v_{ph}(v_{ph}^2 - 1)^2$. The program PTArcade and the 15-year NANOGrav dataset are used to analyze the modified gravity model for different logarithmic velocity priors and different fixed pulsar distances. For the prior range $\log_{10}(v_{ph}) \in [-1, 1]$, the posterior distribution of v_{ph} confirms that the data supports the GR case. For the $\log_{10}(v_{ph}) \in [-1, 0]$ prior, the simplified ORF is studied alongside the modified gravity ORF. The respective posterior distributions of the amplitude A and the phase velocity v_{ph} exhibit almost no deviation from each other for $v_{ph} \ll 1$, underlining that $\Gamma_{ab}^{\mathrm{SIM}}$ can be used for such phase velocities. A degeneracy in the parameters A and v_{ph} is uncovered. The corresponding posterior distribution is sensitive for the parameter combination $P_X = fL_aA^2v_{ph}(v_{ph}^2 - 1)^2$, coinciding with the proportionality of S_{ab}. The values of P_X are found to all roughly correspond to 4×10^{-31}, constraining the cross-power spectrum to this value, indicating a preference of the PTA data for values of A, v_{ph} and fL_a with $S_{ab} \sim 4 \times 10^{-31}$. These results pave the way for future research to further explore the implications of modified gravity theories on PTA data, using the newly derived simplified ORF for subluminal phase velocities.

Declaration of Academic Integrity

I hereby confirm that this thesis, entitled *Imprint of Subluminal Gravitational Waves in PTA Data*, is solely my own work and that I have used no sources or aids other than the ones stated. All passages in my thesis for which other sources, including electronic media, have been used, be it direct quotes or content references, have been acknowledged as such and the sources cited. I am aware that plagiarism is considered an act of deception which can result in sanction in accordance with the examination regulations.

I consent having my thesis cross-checked with other texts to identify possible similarities and to having it stored in a database for this purpose.

I confirm that I have not submitted the following thesis in part or whole as an examination paper before.

Münster, 29th August 2024

Nina Cordes

Contents

1 **Introduction** 1

2 **Theoretical Foundations** 3

2.1 Overview of General Relativity and Gravitational Waves 3
2.2 Hellings and Downs curve in general relativity 6
2.3 Modified gravity 11
2.3.1 Hellings and Downs curve in Legendre decomposition 11
2.3.2 Resummed Overlap Reduction Function 17
2.3.3 Auto-Correlation 19

3 **Principles of PTA analysis** 23

3.1 PTArcade 23
3.1.1 Bayesian statistics 24
3.1.2 Markov Chain Monte Carlo 25
3.2 Model File Implementation 25

4 **Results** 29

5 **Conclusion and outlook** 33

Appendix 35

Bibliography 37

1 Introduction

Pulsar timing arrays (PTAs) are used to detect and study gravitational waves (GWs) in the nanohertz-frequency band. Pulsars are rotating neutron stars with rotation periods of a few milliseconds, that emit radiation along their magnetic field axes. These pulses can be detected on Earth and due to the stability of the rotation, their arrival times are highly consistent and reproducible, even over the span of decades [1]. Passing gravitational waves cause perturbations in the space-time metric, which in turn affect the arrival time of the pulses. PTA searches aim to detect a characteristic pattern in the cross-correlation of timing residuals from pairs of pulsars, induced by GWs. This pattern is described by the overlap reduction function (ORF) Γ_{ab}.
In general relativity (GR), the ORF corresponds to the Hellings and Downs (HD) curve, to which the foundations were first published by Ron W. Hellings and George S. Downs in 1983 [2]. In 2023, many PTA collaborations presented observational evidence for a gravitational wave background consistent with the HD correlation ([3, 4, 5]), including 15 yr Data Set of the NANOGrav collaboration [6].

It is of interest to explore modifications to general relativity in this context. In modified gravity, dispersion relations associated with subluminal phase velocities or massive gravity can be considered, under which the HD curve receives corrections. This work will focus on the effects of subluminal phase velocities $v_{ph} < 1$.
The theoretical derivation of the HD curve can be approached by different methods, with the analytical approach commonly employed [1, 7]. Another method, also used in the analysis of the cosmic microwave background, involves the decomposition into spherical harmonics [8]. While both derivations are presented in this work, the latter is used to numerically calculate the overlap reduction function in modified gravity and analyze its effects [9, 10]. The focus of previous works on the modified gravity and PTA analyses has primarily been the cross-correlation $\Gamma_{a\neq b}$ between two pulsars, emphasizing the corrections to the HD curve. However, the auto-correlation $\Gamma_{a=b}$, or the correlation of a pulsar with itself, appears to diverge when considering, for example, subluminal phase velocities [11]. Recently published work [12] shows, that an analytical expression for the auto-correlation coefficient can be derived, demonstrating that the divergence is unphysical. In addition, it can be shown that Γ_{aa} scales linearly with the fixed pulsar distance, and for sufficiently small phase velocities, Γ_{aa} provides a good approximation for the model, while the cross-correlations become negligible.

The structure of this work is as follows. In Chapter 2, the theoretical foundations of gravitational waves and pulsar timing arrays are introduced and discussed in detail. This includes the derivation of the Hellings and Downs curve in general relativity, and, in application to modified gravity, the derivation through spherical harmonics. Additionally, the necessary re-summation of the result in Legendre polynomials is discussed. Finally, the analytical expression for the auto-correlation coefficient is presented, along with the resulting simplified ORF for subluminal phase velocities. In Chapter 3, a brief introduction to the implementation of the theoretical results is given. This includes an introduction to the program PTArcade, which is used to analyze new physics models with the 15 year NANOGrav data set. The model code is provided and explained. In Chapter 4 the corner plots of the resulting posterior distributions for different logarithmic phase velocity priors and varying pulsar distance are presented. A comparison between the results of the modified gravity ORF and the simplified ORF is made.

2 Theoretical Foundations

2.1 Overview of General Relativity and Gravitational Waves

The following section gives a brief introduction principles of general relativity GR, with reference to Carroll [13]. The deviation of gravitational waves as metric perturbations is discussed, primarily based on the work of Taylor [1] .

In the theory of GR, gravity is the effect caused by the curvature of four-dimensional space time, also called Minkowski space.
A metric can be defined to simplify the calculation of the space-time interval $(\Delta s)^2$ between two points in space time :

$$(\Delta s)^2 = c(\Delta t)^2 - (\Delta x)^2 - (\Delta y)^2 - (\Delta z)^2 = c(\Delta t)^2 - (\Delta \ell)^2 \tag{2.1}$$

$$= \sum_{\mu=0}^{3} \sum_{\nu=0}^{3} \eta_{\mu\nu} \Delta x_\mu \Delta x_\nu. \tag{2.2}$$

Where c corresponds to the speed of light and acts as a fixed conversion factor between the time dimension and the dimensions of space. The indices μ and ν run over the temporal and spatial coordinates. The metric tensor $\eta_{\mu\nu}$, also called the Minkowski tensor, is a 4x4 matrix with entries on the main diagonal:

$$\eta_{\mu\nu} = \begin{pmatrix} 1 & 0 & 0 & 0 \\ 0 & -1 & 0 & 0 \\ 0 & 0 & -1 & 0 \\ 0 & 0 & 0 & -1 \end{pmatrix}. \tag{2.3}$$

Establishing the Minkowski metric provides a foundation to understanding how perturbations within this framework lead to gravitational waves.

The mathematical description of gravitational waves is derived from the four dimensional Minkowski spacetime and the Einstein field equations. The Einstein field equations are

$$G_{\mu\nu} \equiv R_{\mu\nu} - \frac{1}{2} R\, g_{\mu\nu} = 8\pi\, T_{\mu\nu}, \tag{2.4}$$

where $R_{\mu\nu}$ is the Ricci tensor, $G_{\mu\nu}$ the Einstein tensor, $T_{\mu\nu}$ the energy stress tensor and $g_{\mu\nu}$ the metric.
Adding a perturbation $h_{\mu\nu}$ to the metric:

$$g_{\mu\nu} = \eta_{\mu\nu} + h_{\mu\nu}, \tag{2.5}$$

with the weak field case $|h_{\mu\nu}| << 1$. Now the Einstein tensor can be expanded to linear order in $h_{\mu\nu}$ and the trace-reversed perturbation can be defined as:

$$\bar{h}_{\mu\nu} = h_{\mu\nu} - n_{\mu\nu}\frac{h}{2} \qquad \bar{h} = -h \quad \text{with} \quad h = \eta^{\mu\nu}h_{\mu\nu}. \tag{2.6}$$

This, with the expansion, results in the following expression of the Einstein tensor:

$$G_{\mu\nu} = \frac{1}{2}\left(\partial_\mu\partial^\alpha\bar{h}_{\alpha_\nu} + \partial_\nu\partial^\alpha\bar{h}_{\alpha\nu} - \Box\bar{h}_{\mu\nu} - \eta_{\mu\nu}\partial^\alpha\partial^\beta\bar{h}_{\alpha\beta}\right) \tag{2.7}$$

with

$$\partial_\mu \equiv \frac{\partial}{\partial x^\mu} \qquad \partial^\mu \equiv \eta^{\mu\nu}\partial_\nu \qquad \Box = \eta^{\mu\nu}\partial_\mu\partial_\nu. \tag{2.8}$$

The metric perturbation $h_{\mu\nu}$ is a 4x4 matrix with 10 degrees of freedom. Gauge fixing can be used to remove spurious degrees of freedoms in the Einstein equations. First a coordinate transformation is performed according to:

$$x^\alpha \to x^\alpha + \xi^\alpha, \tag{2.9}$$

$$h_{\mu\nu} \to h_{\mu\nu} - (\partial_\mu\xi_\nu + \partial_\nu\xi_\mu). \tag{2.10}$$

In this transformation the condition of the weak field case is kept, as $\partial_\mu\xi_\nu$ is of the same order as $|h_{\mu\nu}|$.

By choosing the Lorenz gauge with $\partial^\nu\bar{h}_{\mu\nu} = 0$ the degrees of freedom can be lowered from 10 to 6. The Einstein tensor and the field equation respectively reduce to:

$$G_{\mu\nu} - \frac{1}{2}\Box\bar{h}_{\mu\nu}, \qquad \Box\bar{h}_{\mu\nu} = -16\pi T_{\mu\nu}. \tag{2.11}$$

Under the condition that ξ^μ satisfies the wave equation ($\Box\xi_\mu = 0$), the Lorenz gauge is invariant under a coordinate transformation $x^\mu \to x^\mu + \xi_\mu$. This condition also indicates that $\Box\xi_{\mu,\nu} = 0$. Next, the $\xi_{\mu\nu}$, are subtracted from the 6 components of $\bar{h}_{\mu\nu}$. Due to the dependence of $\xi_{\mu\nu}$ on four independent functions of ξ^μ, the degrees of freedom can be reduced from 6 to 2. The information of gravitational waves are contained in the 2 remaining, independent components of the metric perturbation.

The transverse-traceless (TT) gauge can be defined by the following properties:

$$h^{0\mu} = 0, \quad h^i_i = 0, \quad \partial^j h_{ij} = 0. \tag{2.12}$$

These properties result from requiring that $\bar{h}_{\mu\nu}$ fulfills $\bar{h} = 0$ and $h^{0i} = 0$. Ultimately, without loss of generality, the coordinate system can be chosen so that the gravitational wave is a plane wave propagating along the z-direction. The solution of the wave equation $\Box \bar{h}_{\mu\nu} = 0$ is then:

$$h_{\mu\nu}^{TT}(t,z) = \begin{pmatrix} 0 & 0 & 0 & 0 \\ 0 & h_+ & h_\times & 0 \\ 0 & h_\times & -h_+ & 0 \\ 0 & 0 & 0 & 0 \end{pmatrix} \cos\big(\omega_{GW}(t-z)\big). \tag{2.13}$$

The two degrees of freedom in the metric perturbation correspond to the two polarizations of gravitational waves with the amplitudes h_+ and $h_\times$, also known as ''plus'' and ''cross'' modes. These terms describe how spacetime is deformed by a passing gravitational wave with the respective polarization. The $+$-polarization effects the spacetime such that distances in the x-direction are lengthened and distances in the y-direction are contracted. The $\times$-polarization causes an analogous effect but rotated by $45°$ along the xy-plane. This is illustrated in Figure 2.1.

With the foundations of gravitational waves established, the next chapter will implement this groundwork to derive the Hellings and Downs curve.

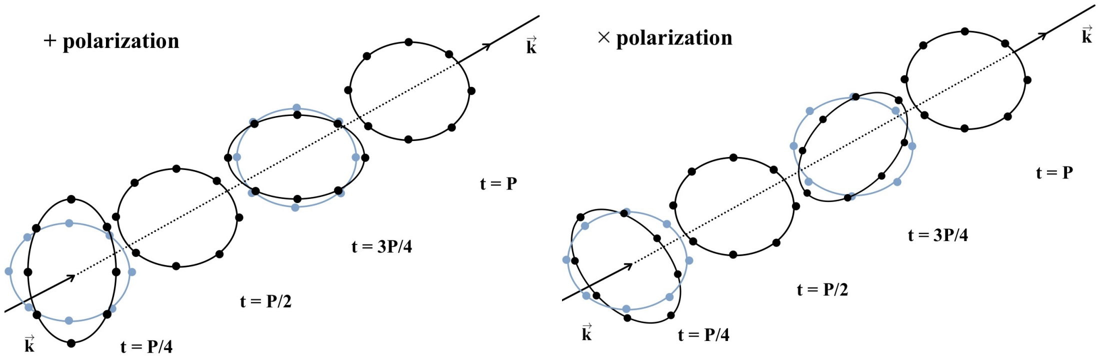

Figure 2.1: Illustration of the deformation of spacetime caused by a passing gravitational wave, with the effects of the two different polarizations $+$ and $\times$. The black dots show how the positions of the particles are affected over time, the blue dots and lines represent the unperturbed positions. Figure is based on [14].

2.2 Hellings and Downs curve in general relativity

The analytical derivation of the HD curve closely follows the method presented in Chapter 23 of Maggiore [7]. To begin, the effect of gravitational waves on the signal timing of one pulsar is considered. As mentioned before, the arrival times of the radio pulses can be predicted and measured with a very high precision. The considered reference frame has the Earth at the origin of the coordinate system and the pulsar a lies in the direction of the unit vector $\hat{\boldsymbol{p}}_a$. The propagation direction of the gravitational wave is denoted by $\hat{\boldsymbol{\Omega}}$. For this initial calculation, where only one pulsar is considered, the unit vector $\hat{\boldsymbol{p}}_a$ can be set to x. Thus, without the loss of generality, the pulsar lies along the x-axis in the direction d_a.
The positions of the Earth and pulsar fixed, as these computations take place in the TT gauge. Thus, the effect of the gravitational wave is limited to the light signal passing between these two points. For $c = 1$ the space time interval is:

$$ds^2 = -(dt)^2 - (dl)^2 = -(dt)^2 + [\delta_{ij} + h_{ij}(t, \boldsymbol{x})]dx^i dx^j. \tag{2.14}$$

The light is travelling from the pulsar ($\boldsymbol{x} = d_a \hat{\boldsymbol{x}}$) to the Earth ($\boldsymbol{x} = 0$), in this coordinate system it moves in the $-\hat{\boldsymbol{x}}$ direction and along a null geodesic ($ds = 0$):

$$dx^2 = \frac{dt^2}{1 + h_{xx}(t, \boldsymbol{x}(t))}, \tag{2.15}$$

$$dx = -\frac{dt}{[1 + h_{xx}(t, \boldsymbol{x}(t))]^{1/2}}. \tag{2.16}$$

The second equality can be approximated to second order:

$$dx = -dt\left[1 - \frac{1}{2}h_{xx}(t, \boldsymbol{x}(t))\right]. \tag{2.17}$$

Using the equations for a long arm interferometer ([15, Chapter 9]), the following expression for the distance between the Earth an pulsar can be derived:

$$L_a = t_{obs} - t_{em} - \frac{1}{2}\int_{t_{em}}^{t_{obs}} dt' h_{xx}(t, \boldsymbol{x}(t')). \tag{2.18}$$

From this, the time at with the light reaches the observer, in this case Earth, can be calculated as:

$$t_{obs} = t_{em} + L_a + \frac{p_a^i p_a^j}{2}\int_{t_{em}}^{t_{em}+L_a} dt'\, h_{ij}\left(t', (t_{em} + L_a - t')\,\hat{\boldsymbol{p}}_a\right). \tag{2.19}$$

The expression of the metric perturbation has been replaced by $p_a^i p_a^j\, h_{ij}$, because in general, the direction of the pulsar does not necessary lie on the x axis. Also, because the path along which the light travels is unperturbed, the function $x(t)$ is equal to $(t_{obs} - t)\hat{\boldsymbol{p}}_a$. The resulting dependency of the metric perturbation on t_{obs} is replaced by the zeroth order expansion: $t_{obs} = t_{em} + L_a$. This substitution is possible in the the integral to first order, as h_{ij} is sufficiently small.

Equation (2.19) is now examined in the context of one whole rotational period (T_a) of the pulsar. The emission time is then: $t'_{em} = t_{em} + T_a$. Replacing $t' = t'' + T_a$ and renaming the integration variable t'' as t' the following expression is obtained:

$$t'_{obs} = t_{em} + T_a + L_a + \frac{p_a^i p_a^j}{2} \int_{t_{em}}^{t_{em}+L_a} dt'\, h_{ij}\left(t' + T_a, (t_{em} + L_a - t')\, \hat{\boldsymbol{p}}_a\right). \tag{2.20}$$

Subtracting 2.19 from 2.20:

$$t'_{obs} - t_{obs} = T_a + \frac{p_a^i p_a^j}{2} \int_{t_{em}}^{t_{em}+L_a} dt' \, \left[h_{ij}\left(t' + T_a, \boldsymbol{x}_0(t')\right) - h_{ij}\left(t', \boldsymbol{x}_0(t')\right)\right] \tag{2.21}$$

with

$$\boldsymbol{x}_0(t') = (t_{em} + L_a - t')\, \hat{\boldsymbol{p}}_a. \tag{2.22}$$

The right side of Eq. (2.21) denotes the time interval at which the signals of the pulsar are seen at Earth. The second part of the left sum, is induced by the passing gravitational wave and can be labeled as ΔT_a. The rotational period of the studied pulsars is usually of the order of a few milliseconds. The period of the gravitational wave (T_{GW}) however, is of the order of one to ten years. With the relation $T_{GW} = \frac{2\pi}{\omega_{GW}}$, it follows that $T_a\omega_{GW}$ is very small. This allows a Taylor-expansion of T_a within the metric perturbation $h_{ij}\left(t' + T_a, \boldsymbol{x}_0(t')\right)$ in Eq. (2.21). To first order this yields:

$$h_{ij}\left(t' + T_a, \boldsymbol{x}_0(t')\right) \approx h_{ij}\left(t', \boldsymbol{x}_0(t')\right) + T_a \frac{\partial}{\partial t} h_{ij}\left(t', \boldsymbol{x}_0(t')\right) + \mathcal{O}(T_a). \tag{2.23}$$

This expansion can be substituted in Eq. (2.21), where the first term $h_{ij}\left(t', \boldsymbol{x}_0(t')\right)$ cancels with the second term of the integral. Dividing by T_a the expression becomes:

$$\frac{\Delta T_a}{T_a} = \frac{p_a^i p_a^j}{2} \int_{t_{em}}^{t_{em}+L_a} dt' \left[\frac{\partial}{\partial t'} h_{ij}\left(t', x\right)\right]_{x=\boldsymbol{x}_0(t')}. \tag{2.24}$$

A, in the $\hat{\boldsymbol{\Omega}}$ direction propagating, monochromatic gravitational wave can be described through [15]:

$$h_{ij}(t, \boldsymbol{x}) = \mathcal{A}_{ij}(\hat{\boldsymbol{\Omega}}) \cos(\omega_{GW}(t - \hat{\boldsymbol{\Omega}} \cdot \boldsymbol{x}/c)). \tag{2.25}$$

This can be substituted into Eq. (2.24) and carrying out the integration yields:

$$\begin{aligned}\frac{\Delta T_a}{T_a} &= \frac{p_a^i p_a^j}{2}\int_{t_{em}}^{t_{em}+L_a} dt' \left[\frac{\partial}{\partial t'}\mathcal{A}_{ij}(\hat{\mathbf{\Omega}})\cos\Big(\omega_{GW}(t'-\hat{\mathbf{\Omega}}\cdot\boldsymbol{x}(t')/c)\Big)\right]_{\boldsymbol{x}=\boldsymbol{x}_0(t')} \\ &= \frac{p_a^i p_a^j}{2}\mathcal{A}_{ij}(\hat{\mathbf{\Omega}})\int_{t_{em}}^{t_{em}+L_a} dt' \left[-\omega_{GW}\sin\Big(\omega_{GW}(t'-\hat{\mathbf{\Omega}}\cdot\hat{\boldsymbol{p}}_a(L_a+t_{em}-t_{obs})/c)\Big)\right] \\ &= \frac{p_a^i p_a^j}{2(\hat{\mathbf{\Omega}}\cdot\hat{\boldsymbol{p}}_a/c+1)}\mathcal{A}_{ij}(\hat{\mathbf{\Omega}})\Bigg[\cos\Big(\omega_{GW}(t_{obs}-\hat{\mathbf{\Omega}}\cdot\hat{\boldsymbol{p}}_a(L_a+t_{em}-t_{obs})/c)\Big) \\ &\qquad\qquad - \cos\Big(\omega_{GW}(t_{em}-\hat{\mathbf{\Omega}}\cdot\hat{\boldsymbol{p}}_a L_a/c)\Big)\Bigg].\end{aligned} \tag{2.26}$$

With $t_{obs} = t_{em} + L_a$ this reduces to:

$$\frac{\Delta T_a}{T_a} = \frac{p_a^i p_a^j}{2(\hat{\mathbf{\Omega}}\cdot\hat{\boldsymbol{p}}_a/c+1)}\mathcal{A}_{ij}(\hat{\mathbf{\Omega}})\left[\cos(\omega_{GW}\,t_{obs})-\cos(\omega_{GW}(t_{em}-\hat{\mathbf{\Omega}}\cdot\hat{\boldsymbol{p}}_a L_a/c))\right]. \tag{2.27}$$

The redshift $z_a(t)$ is generally defined as:

$$z_a(t) = -\left(\frac{\Delta\nu_a}{\nu_a}\right)(t) = \frac{\Delta T_a}{T_a} \quad \text{with} \quad \nu_a = \frac{1}{T_a}. \tag{2.28}$$

Applying this definition of $z_a(t)$ and the expression for the monochromatic gravitational wave in Eq. (2.25), the redshift can be determined by:

$$\begin{aligned} z_a(t) &= \frac{p_a^i p_a^j}{2(\hat{\mathbf{\Omega}}\cdot\hat{\boldsymbol{p}}_a/c+1)}\left[\mathcal{A}_{ij}(\hat{\mathbf{\Omega}})\cos(\omega_{GW}\,t_{obs})-\mathcal{A}_{ij}(\hat{\mathbf{\Omega}})\cos(\omega_{GW}(t_{em}-\tau_a\hat{\mathbf{\Omega}}\cdot\hat{\boldsymbol{p}}_a/c))\right] \\ &= \frac{p_a^i p_a^j}{2(\hat{\mathbf{\Omega}}\cdot\hat{\boldsymbol{p}}_a/c+1)}\left[h_{ij}(t,0)-h_{ij}(t-L_a,\boldsymbol{x}_a)\right],\end{aligned} \tag{2.29}$$

where $t = t_{obs}$.

The first part of this expression with $h_{ij}(t,0)$ is considered to be the Earth term, as $\boldsymbol{x} = 0$ and t correspond to the time at which the signal is observed on Earth. The second part is called the pulsar term, as $\boldsymbol{x} = \boldsymbol{x}_a = L_a\hat{\boldsymbol{p}}_a$ and t correspond to the time the signal was emitted from the pulsar. This is a key outcome in the derivation of the HD curve. Now, the redshift will be studied for a stochastic gravitational wave background instead of for a single monochromatic gravitational wave.

Such a stochastic background can be described by a superposition of waves of all frequencies coming from all possible directions $\hat{\boldsymbol{\Omega}}$ [15]:

$$h_{ij}(t,\boldsymbol{x}) = \sum_{A=+,\times} \int_{-\infty}^{\infty} df \int d^2\hat{\boldsymbol{\Omega}}\, \tilde{h}_A(f,\hat{\boldsymbol{\Omega}})\, e_{ij}^A(\hat{\boldsymbol{\Omega}})\, e^{-2\pi i f(t-\hat{\boldsymbol{\Omega}}\cdot\boldsymbol{x}/c)} \tag{2.30}$$

with the polarization tensors:

$$\begin{aligned} e_{ij}^{+}(\hat{\boldsymbol{\Omega}}) &= \hat{\boldsymbol{u}}_i\hat{\boldsymbol{u}}_j - \hat{\boldsymbol{v}}_i\hat{\boldsymbol{v}}_j, \\ e_{ij}^{\times}(\hat{\boldsymbol{\Omega}}) &= \hat{\boldsymbol{u}}_i\hat{\boldsymbol{v}}_j + \hat{\boldsymbol{v}}_i\hat{\boldsymbol{u}}_j. \end{aligned} \tag{2.31}$$

Substituting this into the expression for the redshift the result is:

$$\begin{aligned} z_a(t) = \frac{p_a^i p_a^j}{2(\hat{\boldsymbol{\Omega}}\cdot\hat{\boldsymbol{p}}_a/c+1)} \Bigg[&\sum_{A=+,\times} \int_{-\infty}^{\infty} df \int d^2\hat{\boldsymbol{\Omega}}\, \tilde{h}_A(f,\hat{\boldsymbol{\Omega}})\, e_{ij}^A(\hat{\boldsymbol{\Omega}})\, e^{-2\pi i f t)} \\ &- \sum_{A=+,\times} \int_{-\infty}^{\infty} df \int d^2\hat{\boldsymbol{\Omega}}\, \tilde{h}_A(f,\hat{\boldsymbol{\Omega}})\, e_{ij}^A(\hat{\boldsymbol{\Omega}})\, e^{-2\pi i f(t-L_a-\hat{\boldsymbol{\Omega}}\cdot\hat{\boldsymbol{p}}_a L_a/c)} \Bigg] \\ = \sum_{A=+,\times} \int_{-\infty}^{\infty} df e^{-2\pi i f t} &\int d^2\hat{\boldsymbol{\Omega}}\, F_a^A(\hat{\boldsymbol{\Omega}})\, \tilde{h}_A(f,\hat{\boldsymbol{\Omega}}) \left[1 - e^{-2\pi i f L_a(1+\hat{\boldsymbol{\Omega}}\cdot\hat{\boldsymbol{p}}_a/c)}\right]. \end{aligned} \tag{2.32}$$

Where the last equation was simplified by defining the detector pattern functions:

$$F_a^A(\hat{\boldsymbol{\Omega}}) = \frac{p_a^i p_a^j}{2(\hat{\boldsymbol{\Omega}}\cdot\hat{\boldsymbol{p}}_a/c)}\, e_{ij}^A(\hat{\boldsymbol{\Omega}}). \tag{2.33}$$

To acquire an expression for the correlation function of the redshift the following average is calculated:

$$\begin{aligned} \langle z_a(t,\hat{\boldsymbol{p}}_a) z_b(t,\hat{\boldsymbol{p}}_b)\rangle = \frac{2}{3} \int_{-\infty}^{\infty} df S_h(f) \int d^2\hat{\boldsymbol{\Omega}} &\left[1 - e^{-2\pi i f L_a(1+\hat{\boldsymbol{\Omega}}\cdot\hat{\boldsymbol{p}}_a/c)}\right] \\ \times \left[1 - e^{2\pi i f L_b(1+\hat{\boldsymbol{\Omega}}\cdot\hat{\boldsymbol{p}}_b/c)}\right] &\sum_{A=+,\times} F_a^A(\hat{\boldsymbol{\Omega}}) F_b^A(\hat{\boldsymbol{\Omega}}). \end{aligned} \tag{2.34}$$

Where $S_h(f)$ is the spectral density of the stochastic gravitational wave background, also referred to as the strain power spectrum:

$$\langle \tilde{h}_A^*(f,\hat{\boldsymbol{\Omega}}) \tilde{h}'_A(f',\hat{\boldsymbol{\Omega}}')\rangle = \frac{1}{8\pi} S_h(f)\delta(f-f')\delta_{AA'}\delta^2(\hat{\boldsymbol{\Omega}},\hat{\boldsymbol{\Omega}}'). \tag{2.35}$$

The integral over $\hat{\mathbf{\Omega}}$ in Eq. (2.34) including all its terms is called the overlap reduction function $\Gamma_{ab}(f,\xi)$.
In the GR limit, the two terms in the square bracket in Eq. (2.34) go to one, as the two exponential factors result in two fast oscillating terms, which in return are negligible when preforming the integration [12]. Thus the overlap reduction function reduces to:

$$\Gamma_{ab}^{\mathrm{HD}}(f,\xi) = \frac{3}{2}\frac{1}{4\pi}\int d^2\hat{\mathbf{\Omega}} \sum_{A=+,\times} F_a^A(\hat{\mathbf{\Omega}})F_b^A(\hat{\mathbf{\Omega}}), \tag{2.36}$$

where ξ denotes the angular separation of pulsars a and b and the upper index "HD" serves to differentiate this ORF from others derived in the following sections.
The unit vectors of the polarization tensors in Eq. (2.32) can be specified in such a way that they are orthogonal to $\hat{\mathbf{\Omega}}$ and to each other:

$$\begin{aligned} \hat{\boldsymbol{u}} &= (\sin\phi, -\cos\phi, 0) \\ \hat{\boldsymbol{v}} &= (\cos\theta\cos\phi, \cos\theta\sin\phi, -\sin\theta) \\ \text{and}\quad \hat{\mathbf{\Omega}} &= (\sin\theta\cos\phi, \sin\theta\sin\phi, \cos\theta). \end{aligned} \tag{2.37}$$

The chosen reference frame is the ''computational'' frame, where pulsar a is located on the z-axis and pulsar b in the xz-plane [8]:

$$\hat{\boldsymbol{p}}_a = (0,0,01) \tag{2.38}$$

$$\hat{\boldsymbol{p}}_b = (\sin\xi, 0, \cos\xi) \tag{2.39}$$

With this, the integral in Eq. (2.36) can be computed analytically. One of the key steps is identifying, that the terms of the cross polarization $F^\times$ vanish because $\hat{\boldsymbol{p}}\cdot\hat{\boldsymbol{u}} = 0$ [16]. The expression can then be split into multiple integrals over θ and ϕ and solved using contour integration and the residue theorem [17]. The result is the HD curve:

$$\Gamma_{ab}^{\mathrm{HD}}(f,\xi) = \frac{3}{2}x_{ab}\log(x_{ab}) - \frac{1}{4}x_{ab} + \frac{1}{2} \quad x_{ab} = \frac{1}{2}(1-\cos\xi_{ab}). \tag{2.40}$$

The detailed calculation is not included here, as it does not directly contribute to the further discussions. Instead, the focus is on how the results are affected by modified gravity, which will be examined in the following chapter.

2.3 Modified gravity

In modified gravity, the derived overlap reduction function is applied to theories that go beyond general relativity. For subluminal phase velocities $v_{ph} < 1$ this means that the dispersion relation takes the form:

$$\omega(k) = v_{ph}k, \quad k = |\mathbf{k}|. \tag{2.41}$$

For this scenario the group velocity $v_{gr} = \partial\omega/\partial k$ and the phase velocity are equal. This linear dispersion relation sets a limit on the phase velocity: if v_{ph} would be assumed to be larger than 1, then this would also apply to v_{gr}. However, the group velocity cannot be larger than $c = 1$. As this leads to a violation of causality and a nonphysical result.

In addition, for subluminal phase velocities the exponential factors in Eq. (2.34) can no longer be set to zero, as this would result in a intrinsic singularity at $v_{ph} = \hat{\boldsymbol{\Omega}} \cdot \hat{\boldsymbol{p}}$ [10]. Here the decomposition into spherical harmonics and the resulting expression in Legendre polynomials proves to be advantageous, as it allows a numerical evaluation of the overlap reduction function.

2.3.1 Hellings and Downs curve in Legendre decomposition

The derivation using spherical harmonics closely follows the work of Gair et al. [8] and Liang et al. [10]. In the previous section the polarization tensors (Eq. (2.32)) and unit vectors (Eq. (2.38)) were introduced. To project the gravitational wave onto a sphere in three dimensions with a fixed radius, a change in coordinates is preformed from Cartesian to spherical. Through this, the gravitational wave can now be expressed in two dimensions. The unit vectors and polarization tensors are:

$$\begin{aligned} \hat{\boldsymbol{u}} = \hat{\boldsymbol{\phi}} \quad \hat{\boldsymbol{v}} &= \hat{\boldsymbol{\theta}} \quad \hat{\boldsymbol{\Omega}} = \hat{\boldsymbol{r}} \\ e^{+}_{ab}(\hat{\boldsymbol{\Omega}}) &= \hat{\boldsymbol{\phi}}_a\hat{\boldsymbol{\phi}}_b - \hat{\boldsymbol{\theta}}_a\hat{\boldsymbol{\theta}}_b \\ e^{\times}_{ab}(\hat{\boldsymbol{\Omega}}) &= \hat{\boldsymbol{\phi}}_a\hat{\boldsymbol{\theta}}_b + \hat{\boldsymbol{\theta}}_a\hat{\boldsymbol{\phi}}_b \end{aligned} \tag{2.42}$$

As used in the analysis of CMB signals, the rank-2 tensors on the two dimensional sphere can be decomposed into spherical harmonics. For the following steps, it is convenient to define the curl and gradient of the spherical harmonics:

$$\begin{aligned} \text{gradient: } Y^{G}_{(\ell m)ab} &= N_\ell\Big(Y_{(\ell m);ab} - \frac{1}{2}g_{ab}Y_{(\ell m);c}{}^{c}\Big) \\ \text{curl: } Y^{C}_{(\ell m)ab} &= \frac{N_\ell}{2}\Big(Y_{(\ell m);ac}\epsilon^{c}_{b} + Y_{(\ell m);bc}\epsilon^{a}_{c}\Big) \end{aligned} \tag{2.43}$$

Here g_{ab} is the metric tensor on the sphere and the semi colon indicates covariant differentiation. N_l is defined as:

$$N_l = \sqrt{\frac{2(\ell-2)!}{(\ell+2)!}}. \tag{2.44}$$

From these definitions the Fourier components of the metric perturbation $h_{ab}(f, \hat{\mathbf{\Omega}})$ can be expressed as:

$$h_{ab}(f, \hat{\mathbf{\Omega}}) = \sum_{\ell=2}^{\infty} \sum_{m=-\ell}^{\ell} \left[a^G_{(\ell m)}(f) Y^G_{(\ell m)ab}(\hat{\mathbf{\Omega}}) + a^C_{(\ell m)}(f) Y^C_{(\ell m)ab}(\hat{\mathbf{\Omega}}) \right]. \tag{2.45}$$

with:

$$\begin{aligned} a^C_{(\ell m)}(f) &= \int_{S^2} d^2\hat{\mathbf{\Omega}}\ h_{ab}(f, \hat{\mathbf{\Omega}}) {Y^C_{(\ell m)}}^{ab*}(\hat{\mathbf{\Omega}}), \\ a^G_{(\ell m)}(f) &= \int_{S^2} d^2\hat{\mathbf{\Omega}}\ h_{ab}(f, \hat{\mathbf{\Omega}}) {Y^G_{(\ell m)}}^{ab*}(\hat{\mathbf{\Omega}}). \end{aligned}$$

The summation over starts at $\ell = 2$, as the monopole ($\ell = 0$) and dipole ($\ell = 1$) contributions vanishes for gravitational waves far from the source and the leading-order term of the gravitational wave radiation is the quadrupole moment [18]. The spherical harmonics indices are differentiated form the spatial tensor indices by parentheses.

Substituting the new decomposition Eq. (2.45) into Eq. (2.30) the metric perturbation induced by a stochastic gravitational wave background is:

$$h_{ab}(t, \boldsymbol{x}) = \int_{-\infty}^{\infty} df \int d^2\hat{\mathbf{\Omega}} \left\{ \sum_{(m\ell)} \left[a^G_{(\ell m)}(f) Y^G_{(\ell m)ab}(\hat{\mathbf{\Omega}}) + a^C_{(\ell m)}(f) Y^C_{(\ell m)ab}(\hat{\mathbf{\Omega}}) \right] \right\} e^{-2\pi i f (t - \frac{\hat{\mathbf{\Omega}} \cdot \boldsymbol{x}}{v_{ph}})}. \tag{2.46}$$

The spherical harmonics can be written as:

$$\begin{aligned} Y^G_{(\ell m)ab}(\hat{\mathbf{\Omega}}) &= \frac{N_\ell}{2} \left[W_{(\ell m)}(\hat{\mathbf{\Omega}}) e^+_{ab}(\hat{\mathbf{\Omega}}) + X_{(\ell m)}(\hat{\mathbf{\Omega}}) e^\times_{ab}(\hat{\mathbf{\Omega}}) \right], \\ Y^C_{(\ell m)ab}(\hat{\mathbf{\Omega}}) &= \frac{N_\ell}{2} \left[W_{(\ell m)}(\hat{\mathbf{\Omega}}) e^\times_{ab}(\hat{\mathbf{\Omega}}) - X_{(\ell m)}(\hat{\mathbf{\Omega}}) e^+_{ab}(\hat{\mathbf{\Omega}}) \right], \end{aligned} \tag{2.47}$$

breaking them down into terms of the cross and plus polarization. This can also be done for the metric perturbation and it follows:

$$h_{ab}(t, \boldsymbol{x}) = \int_{-\infty}^{\infty} df \int d^2\hat{\mathbf{\Omega}} \left[h^+(f, \hat{\mathbf{\Omega}}) e^+_{ab}(\hat{\mathbf{\Omega}}) + h^\times(f, \hat{\mathbf{\Omega}}) e^\times_{ab}(\hat{\mathbf{\Omega}}) \right] e^{-2\pi i f (t - \frac{\hat{\mathbf{\Omega}} \cdot \boldsymbol{x}}{v_{ph}})}, \tag{2.48}$$

with

$$h_+(f,\hat{\boldsymbol{\Omega}}) = \sum_{(lm)} \frac{N_l}{2} \left[a^G_{(lm)}(f)W_{(lm)}(\hat{\boldsymbol{\Omega}}) - a^C_{(lm)}(f)X_{(lm)}(\hat{\boldsymbol{\Omega}})\right], \tag{2.49}$$

$$h_\times(f,\hat{\boldsymbol{\Omega}}) = \sum_{(lm)} \frac{N_l}{2} \left[a^G_{(lm)}(f)X_{(lm)}(\hat{\boldsymbol{\Omega}}) + a^C_{(lm)}(f)W_{(lm)}(\hat{\boldsymbol{\Omega}})\right]. \tag{2.50}$$

Where $W_{(lm)}$ and $X_{(lm)}$ are defined as [19]:

$$W_{(lm)} \equiv \left(2\frac{\partial^2}{\partial\theta^2} + \ell(\ell+1)\right) Y_{(lm)}, \tag{2.51}$$

$$X_{(lm)} \equiv \frac{2im}{\sin\theta}\left(\frac{\partial}{\partial\theta} - \cot\theta\right) Y_{(lm)}. \tag{2.52}$$

From the definition of the strain power spectrum $S_h(f)$ in Eq. (2.35) and the definitions in Eq. (2.46) follows:

$$\left\langle a^G_{(\ell m)}(f)a^{G*}_{(\ell' m')}\left(f'\right)\right\rangle = \left\langle a^C_{(\ell m)}(f)a^{C*}_{(\ell' m')}\left(f'\right)\right\rangle = S_h(f)\delta_{\ell\ell'}\delta_{mm'}\delta\left(f-f'\right). \tag{2.53}$$

Returning to the redshift and timing residuals defined in Sec. 2.2, the expression for the timing residual in modified gravity is:

$$r(t) = \int_0^t z\left(t'\right)dt' = \int_{-\infty}^{\infty} \frac{df e^{2\pi i f t}}{2\pi i f} \int d^2\hat{\boldsymbol{\Omega}} \frac{\hat{\boldsymbol{p}}^a\hat{\boldsymbol{p}}^b h_{ab}}{2\left(1+\frac{\hat{\boldsymbol{\Omega}}\cdot\hat{\boldsymbol{p}}}{v_{ph}}\right)}\left(1 - e^{-2\pi i f L(1+\hat{\boldsymbol{\Omega}}\cdot\hat{\boldsymbol{p}}/v_{ph})}\right) \tag{2.54}$$

The metric pertubation can be decomposed into the basis of the spherical harmonics (Eq. (2.45)). In this decomposition, the detector response function $R^P(f,\hat{\boldsymbol{\Omega}})$ can be defined as:

$$r(t) = \int_{-\infty}^{\infty} df e^{2\pi i f t} \int d^2\hat{\boldsymbol{\Omega}} \sum_{(\ell m)} \sum_{P=G,C} R^P(f,\hat{\boldsymbol{\Omega}})a^P_{(\ell m)}(f). \tag{2.55}$$

Comparing these expressions above with the decomposition of the metric perturbation, the detector response function is:

$$R^P_{(lm)}(f) = \frac{1}{i2\pi f}\int d^2\hat{\boldsymbol{\Omega}} \frac{p^a p^b}{2(1+\frac{\hat{\boldsymbol{\Omega}}\cdot\hat{\boldsymbol{p}}}{v_{ph}})} Y^P_{(lm)ab}(\hat{\boldsymbol{\Omega}})e^{-i2\pi f t}\left[1 - e^{-i2\pi f L(1+\hat{\boldsymbol{\Omega}}\cdot\hat{\boldsymbol{p}}/v_{ph})}\right] \tag{2.56}$$

As in the previous section, the correlation function of the redshift of two pulsars a and b is calculated. Using Eqs. (2.55), (2.56) and the definition of the strain power spectrum in Eq. (2.53) it follows:

$$\langle r(t, \hat{\boldsymbol{p}}_a)\, r(t', \hat{\boldsymbol{p}}_b)\rangle = \int_{-\infty}^{\infty} df e^{2\pi i f(t-t')} S_h(f) \Gamma_{ab}(f, \xi_{ab}). \tag{2.57}$$

Where $\Gamma_{ab}(f, \xi_{ab})$ is once again the overlap reduction function and ξ the angular separation of the two vectors. In the harmonic basis the ORF is:

$$\Gamma_{ab}(f, \xi_{ab}) = \mathcal{C} \sum_{(\ell m)} \sum_{P=G,C} R^{P}_{(lm)}(f, \hat{\boldsymbol{p}}_a) R^{P*}_{(lm)}(f, \hat{\boldsymbol{p}}_b). \tag{2.58}$$

In Eq. (2.39) the ''computational'' reference frame was used to calculate the overlap reduction function. It is also possible to calculate $\Gamma_{ab}(f, \xi_{ab})$ in a different reference frame, in which both pulsars lie along the z-axis. For this a rotation of coordinates is performed from the initial position of the pulsars: $\hat{\boldsymbol{p}}_{\mathrm{i}} = (\sin\zeta_{\mathrm{i}} \cos\chi_{\mathrm{i}}, \sin\zeta_{\mathrm{i}} \sin\chi_{\mathrm{i}}, \cos(\zeta_{\mathrm{i}})$ to $\bar{\hat{\boldsymbol{p}}} = (0, 0, 1)$ with the associated rotational matrix $\mathbf{R}(\chi_{\mathrm{i}}, \zeta_{\mathrm{i}}, 0)\hat{\boldsymbol{p}}_{\mathrm{i}}$. The direction of the gravitational wave is denoted by $\bar{\hat{\boldsymbol{\Omega}}}$, where $\bar{\hat{\boldsymbol{\Omega}}} \cdot \bar{\hat{\boldsymbol{p}}} = \cos\bar{\theta}$. Using the Wigner-D matrix $D^{\ell}_{mm'}$ the curl and gradient of the spherical harmonics transform as:

$$Y^{P}_{(\ell m)ab}(\theta, \phi) = \sum_{m'=-\ell}^{\ell} \left[D^{\ell}_{mm'}(\chi, \zeta, 0)\right]^{*} Y^{P}_{(\ell m')\bar{a}\bar{b}}\left(\bar{\theta}_{\mathrm{i}}, \bar{\phi}_{\mathrm{i}}\right) \mathbf{R}\left(\chi_{\mathrm{i}}, \zeta_{\mathrm{i}}, 0\right)^{\bar{a}}{}_{a} \mathbf{R}\left(\chi_{\mathrm{i}}, \zeta_{\mathrm{i}}, 0\right)^{\bar{b}}{}_{b}. \tag{2.59}$$

To apply this to the detector response functions, the integral over $\hat{\boldsymbol{\Omega}}$ in $R^{P}_{(lm)}(f, \hat{\mathbf{p}})$ and the spherical harmonics need to be expressed in the angles θ and ϕ:

$$R^{P}_{(\ell m)}(f, \hat{\mathbf{p}}) = \frac{1}{2\pi i f} \int_{-1}^{1} d\cos\theta \int_{0}^{2\pi} d\phi \frac{\hat{p}^a \hat{p}^b}{2(1 + \frac{\hat{\boldsymbol{\Omega}}\cdot\hat{\mathbf{p}}}{v_{ph}})} Y^{P}_{(\ell m)ab}(\theta, \phi) \left[1 - e^{-i2\pi f L\left(1+\hat{\boldsymbol{\Omega}}\cdot\hat{\mathbf{p}}/v_{ph}\right)}\right]. \tag{2.60}$$

The rotation of the gradient and curl can be substituted into the above expression and using Eq. (2.47), the detector response functions for the gradient and curl equal respectively:

$$\begin{aligned} R^{G}_{(\ell m)}(f, \hat{\mathbf{p}}) = {} & \sum_{m'=-\ell}^{\ell} \left[D^{\ell}_{mm'}(\chi, \zeta, 0)\right]^{*} \frac{1}{2\pi i f} \\ & \times \int_{-1}^{1} d\cos\bar{\theta} \int_{0}^{2\pi} d\bar{\phi} \left[1 - e^{-i2\pi f L(1+\cos\bar{\theta})}\right] \frac{\bar{\hat{p}}^a \bar{\hat{p}}^b}{2(1 + \frac{\cos\bar{\theta}}{v_{ph}})} \frac{N_l}{2} \left(W_{\ell m'} e^{+}_{ab} + X_{\ell m'} e^{\times}_{ab}\right), \end{aligned} \tag{2.61}$$

$$R^C_{(\ell m)}(f,\hat{\boldsymbol{p}}) = \sum_{m'=-\ell}^{\ell} \left[D^\ell_{mm'}(\chi,\zeta,0)\right]^* \frac{1}{2\pi i f} \tag{2.62}$$
$$\times \int_{-1}^{1} d\cos\bar{\theta} \int_0^{2\pi} d\bar{\phi} \left[1 - e^{-i2\pi f L(1+\cos\bar{\theta})}\right] \frac{\bar{\hat{p}}^a \bar{\hat{p}}^b}{2(1+\frac{\cos\bar{\theta}}{v_{ph}})} \frac{N_l}{2} \left(W_{\ell m'} e^\times_{ab} - X_{\ell m'} e^+_{ab}\right).$$

Analogously to the previous section the detector pattern functions can be defined as:

$$F^{+,\times}(\bar{\hat{\boldsymbol{\Omega}}}) = \frac{\bar{\hat{p}}^a \bar{\hat{p}}^b}{2(1+\cos\bar{\theta}/v_{ph})} e^{+,\times}_{ab}(\bar{\hat{\boldsymbol{\Omega}}}). \tag{2.63}$$

From this definition and the reference frame implemented above, it becomes clear that the cross-polarization $F^\times(\bar{\hat{\boldsymbol{\Omega}}})$ becomes zero and $F^+(\bar{\hat{\boldsymbol{\Omega}}}) = \frac{1-\cos^2(\bar{\theta})}{2(1+\cos\bar{\theta}/v_{ph})}$. The detector response functions thus reduce to:

$$R^G_{(\ell m)}(f,\hat{\boldsymbol{p}}) = \sum_{m'=-\ell}^{\ell} \left[D^\ell_{mm'}(\chi,\zeta,0)\right]^* \frac{1}{2\pi i f} \tag{2.64}$$
$$\times \int_{-1}^{1} d\cos\bar{\theta} \int_0^{2\pi} d\bar{\phi} \left[1 - e^{-i2\pi f L(1+\cos\bar{\theta})}\right] F^+(\bar{\hat{\boldsymbol{\Omega}}}) \frac{N_l}{2} W_{\ell m'},$$

$$R^C_{(\ell m)}(f,\hat{\boldsymbol{p}}) = \sum_{m'=-\ell}^{\ell} \left[D^\ell_{mm'}(\chi,\zeta,0)\right]^* \frac{1}{2\pi i f} \tag{2.65}$$
$$\times \int_{-1}^{1} d\cos\bar{\theta} \int_0^{2\pi} d\bar{\phi} \left[1 - e^{-i2\pi f L(1+\cos\bar{\theta})}\right] F^+(\bar{\hat{\boldsymbol{\Omega}}}) \frac{N_l}{2} X_{\ell m'}.$$

Both $X_{\ell m'}$ and $W_{\ell m'}$ are proportional to $e^{im'\bar{\phi}}$, this can be seen when expressing them in terms of associated Legendre functions [8]. Due to this proportionality and the orthogonality of the complex exponentials, the integral over $\bar{\phi}$ is zero for every $m' \neq 0$. Now the $R^A_{(\ell m)}$ can be calculated individually. For the gradient (with $x = \cos\theta$):

$$R^G_{(\ell m)}(f,\hat{\boldsymbol{p}}) = \frac{\left[D^\ell_{m0}(\chi,\zeta,0)\right]^*}{2\pi i f} \frac{N_l}{2} \int d^2\hat{\boldsymbol{\Omega}} \left[1 - e^{-i2\pi f L(1+x)}\right] \frac{1-x^2}{2(1+\frac{x}{v_{ph}})} W_{\ell 0}, \tag{2.66}$$

and for the curl:

$$R^C_{(\ell m)}(f,\hat{\boldsymbol{p}}) = \frac{\left[D^\ell_{m0}(\chi,\zeta,0)\right]^*}{2\pi i f} \frac{N_l}{2} \int d^2\hat{\boldsymbol{\Omega}} \left[1 - e^{-i2\pi f L(1+x)}\right] \frac{1-x^2}{2(1+\frac{x}{v_{ph}})} X_{\ell 0} = 0, \tag{2.67}$$

as $X_{\ell 0} = 0$, which follows from Eq. (2.52).

The expression for the gradients detector response function can be simplified by defining the factors c_ℓ:

$$c_\ell(f) \equiv \sqrt{\frac{4}{(2l+1)\pi}} \int d^2\hat{\mathbf{\Omega}} \left[1 - e^{-i2\pi f L\left(1+\frac{1}{v_{ph}}x\right)}\right] \frac{1-x^2}{1+\frac{x}{v_{ph}}} W_{(\ell 0)}(x) \tag{2.68}$$

$$= \int_{-1}^{1} dx \frac{\left(1-x^2\right)^2}{1+\frac{x}{v_{ph}}} \left[1 - e^{-i2\pi f L\left(1+\frac{1}{v_{ph}}x\right)}\right] \frac{d^2}{dx^2} P_\ell(x). \tag{2.69}$$

With the definition of the Wigner D matrix:

$$\left[D^\ell_{m0}(\chi,\zeta,0)\right]^* = \sqrt{\frac{4\pi}{2\ell+1}} Y_{\ell m}(\chi,\zeta), \tag{2.70}$$

the detector response function of the gradient is:

$$R^G_{(\ell m)}(f,\hat{\boldsymbol{p}}) = \frac{\left[D^\ell_{m0}(\chi,\zeta,0)\right]^*}{2\pi i f} \frac{N_\ell}{2} \sqrt{\frac{(2\ell+1)\pi}{4}} c_\ell(f) = \frac{Y_{\ell m}(\chi,\zeta)}{2\pi i f} \frac{N_\ell \pi}{2} c_\ell(f). \tag{2.71}$$

The overlap reduction function in Eq. (2.58) is accordingly:

$$\begin{aligned}\Gamma_{ab}(f,\xi_{ab}) &= \frac{1}{(2\pi f)^2} \sum_{m=-\ell}^{\ell} Y_{\ell m}\left(\chi_a,\zeta_a\right) Y^*_{\ell m}\left(\chi_b,\zeta_b\right) \left(\frac{N_\ell \pi}{2}\right)^2 \left|c_\ell(f)\right|^2 \\ &= \frac{1}{64\pi f^2}(2\ell+1) N_\ell^2 \left|c_\ell(f)\right|^2 P_\ell(\cos\xi_{ab}).\end{aligned} \tag{2.72}$$

The second equality follows from the addition theorem for spherical harmonics [20]:

$$P_\ell(\cos\xi) = \frac{4\pi}{2\ell+1} \sum_{m=-\ell}^{\ell} Y_{\ell m}\left(\chi_a,\zeta_a\right) Y^*_{\ell m}\left(\chi_b,\zeta_b\right). \tag{2.73}$$

The factor in the front of the equation $\frac{1}{64\pi f^2}$ can be added to the definition of the power spectrum, resulting in final expression for the ORF in Legendre polynomials:

$$\Gamma_{ab}(f,\xi_{ab}) = \sum_{\ell=2}^{\infty} a_\ell P_\ell(\cos\xi_{ab}) \quad \text{with} \quad a_\ell \equiv \frac{3}{2}(2\ell+1)\frac{2(\ell-2)!}{(\ell+2)!}|c_\ell(f)|^2. \tag{2.74}$$

Taking the GR limit ($v_{ph} = 1$) of this expression, the exponential factor in the c_ℓ coefficients leads to a damping oscillation and for large fL, the exponential can be dropped. The coefficients then reduce to $c_\ell = (-1)^\ell 4$ and the original Hellings and Downs result can be recovered.

2.3.2 Resummed Overlap Reduction Function

A key detail in the expansion introduced in the previous section is the slow convergence of the Legendre polynomials due to the fact that the coefficients a_ℓ decrease less slowly with increasing ℓ. This has been illustrated in Figure 2.2.

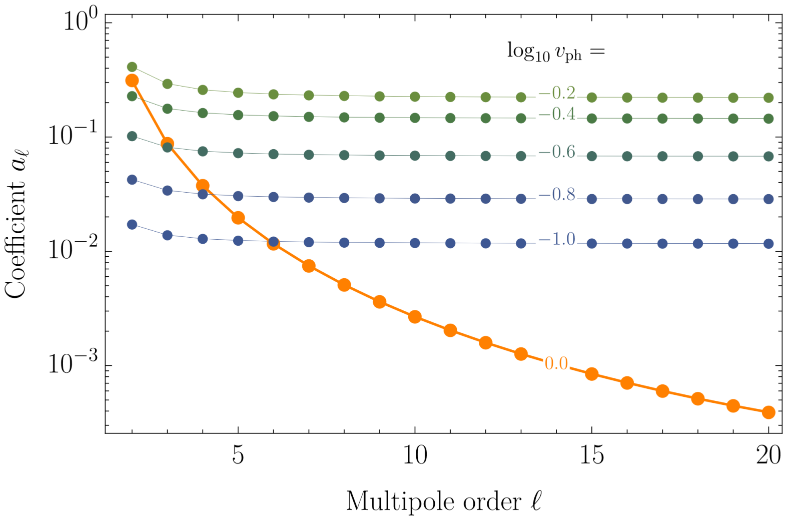

Figure 2.2: The first 20 a_ℓ coefficients of the ORF expressed through Legendre polynomials in Eq. 2.74 for different values of the phase velocity v_{ph}. Figure reproduced from [12].

The discussion of this matter adheres to Liang, Lin, and Trodden [10] and Cordes et al. [12]. Figure 2.3 shows ORF from Eq. (2.74) plotted with an expansion up to $\ell = 20$ ($\Gamma_{ab}^{(20)}$ (ξ_{ab}, f)) for different values of subliminal phase velocities.

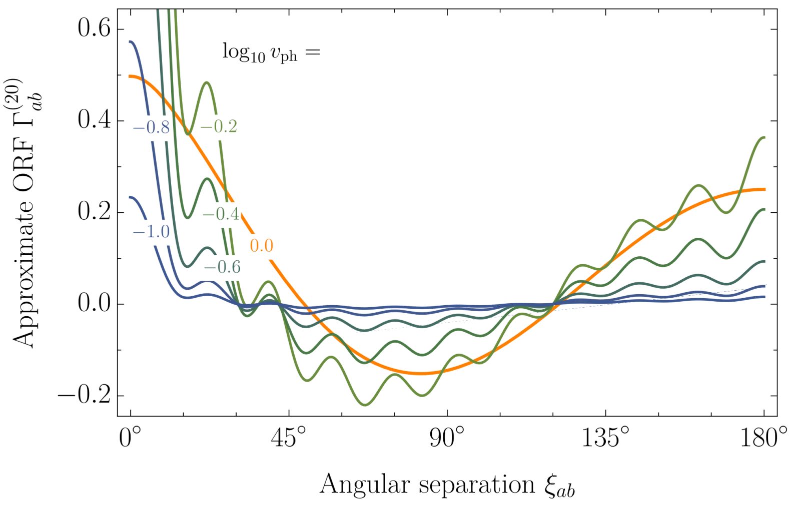

Figure 2.3: The corresponding truncated ORF for different phase velocities, calculated using only the first 20 terms in the decomposition. The orange curve shows the ORF for the GR case. Figure reproduced from [12].

The plot shows that the resulting ORFs do not provide an adequate representation and that improvement of the approximation is necessary. This is done by introducing a second factor where the remaining terms of the Legendre polynomials are summed as follows:

$$\Gamma_{ab}\left(\xi_{ab}, f\right) = \sum_{\ell=2}^{20} a_\ell(f) P_\ell\left(\cos\xi_{ab}\right) + \Theta\left(-\log_{10} v\right) a_{20}(f) \sum_{\ell=21}^{\infty} P_\ell\left(\cos\xi_{ab}\right) \tag{2.75}$$

$$= \Gamma^{(}20)_{ab}\left(\xi_{ab}, f\right) + \Theta\left(-\log_{10} v\right) a_{20}(f) \sum_{\ell=21}^{\infty} P_\ell\left(\cos\xi_{ab}\right). \tag{2.76}$$

With the Heaviside theta function $\Theta(-\log_{10}(v)) = 1$ for $-\log_{10}(v) > 1$ and $\Theta(-\log_{10}(v)) = 0$ for $-\log_{10}(v) \leq 1$. Expressing the bounds of the phase velocity logarithmically is done to cover and thus analyze a wide range of v_{ph} values effectively. The summation can be simplified by using the sum rule for Legendre polynomials:

$$\sum_{\ell=0}^{\infty} P_\ell\left(\cos\xi_{ab}\right) = \frac{1}{\sqrt{2 - 2\cos\xi_{ab}}}. \tag{2.77}$$

In Figure 2.4 the resummed ORF from Eq. (2.78) is plotted. It is clear that this expression gives a much better approximation for the cross-correlation.

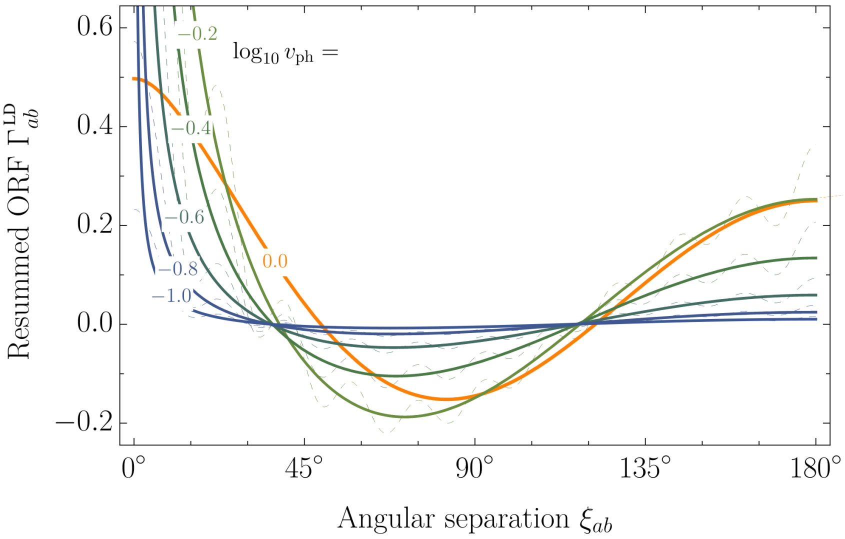

Figure 2.4: The resummed ORF $\Gamma_{ab}^{\mathrm{LD}}$ from Eq. (2.78) compared to the truncated ORF (dashed lines) consisting only of the first $\ell = 20$ terms in Eq. (2.74). The ORFs are plotted for different values of $\log_{10}(v_{ph})$ and orange curve corresponds to the result in general relativity $\Gamma_{ab}^{\mathrm{HD}}$. The resummed ORF shows a significant improvement over the truncated result (adapted from [12]).

The resummed overlap reduction function is:

$$\Gamma_{ab}^{\mathrm{LD}}\left(\xi_{ab}, f\right) = \sum_{\ell=2}^{20} a_\ell(f) P_\ell\left(\cos\xi_{ab}\right) + \Theta\left(-\log_{10} v\right) a_{20}(f)\left[\frac{1}{\sqrt{2-2\cos\xi_{ab}}} - \sum_{\ell=0}^{20} P_\ell\left(\cos\xi_{ab}\right)\right] \tag{2.78}$$

However this approach does not give a satisfying result for the auto-correlation term. As $\xi_{ab} \to \infty$ the term $\sqrt{2-2\cos\xi_{ab}}$ diverges at $\xi_{ab} = 0$. This divergence is problematic, as it is necessary to include the auto-correlation term when analysing PTA data. The power spectrum's ($S_h(f)$ in Eq. (2.35)) sensitivity is derived through Γ_{aa}. The auto-correlation coefficient is much larger that the cross-correlation coefficients ($\xi_{ab} \neq 0$), causing Γ_{aa} to be more sensitive to an initial detection of a signal. The cross-correlations play less of a role in the sensitivity and are more relevant to classifying the gravitational wave signal. This context needs to represented when modeling theories of modified gravity to PTA data. The divergence of Eq. (2.78) at $\xi_{ab} \to \infty$ thus cannot be disregarded. A solution to the calculation of the auto-correlation coefficient is given in the following section.

2.3.3 Auto-Correlation

In Cordes et al. [12] an approach to calculating the auto-correlation coefficient is introduced that does not use the decomposition into Legendre polynomials. Instead, the approach returns to the analytical expressions in Sec. 2.2 and considers the auto-correlation function $\Gamma_{a=b}(f, \xi_{a=b})$. The auto-correlation coefficient for subluminal velocities is then:

$$\begin{aligned}\Gamma_{aa}(f) &= \frac{3}{2}\int \frac{d^2\hat{\mathbf{\Omega}}}{4\pi} \sum_{A=+,\times}\left[1 - e^{-2\pi i f L_a\left(1+\frac{\hat{\mathbf{\Omega}}\cdot\hat{\boldsymbol{p}}_a}{v_{ph}}\right)}\right]\left[1 - e^{2\pi i f L_a\left(1+\frac{\hat{\mathbf{\Omega}}\cdot\hat{\boldsymbol{p}}_a}{v_{ph}}\right)}\right]\left[\frac{p_a^i p_a^j e_{ij}^A(\hat{\mathbf{\Omega}})}{2\left(\frac{\hat{\mathbf{\Omega}}\cdot\hat{\boldsymbol{p}}_a}{v_{ph}}+1\right)}\right]^2 \\ &= \frac{3}{4}\int_0^\infty d\theta\, \frac{\sin^5\theta \sin^2(\pi f L_a(1+\cos\theta/v_{ph}))}{(1+\cos\theta/v_{ph})}.\end{aligned} \tag{2.79}$$

An exact solution of the integral is possible and presented in [12]. Using the following notation:

$$x_\pm = \frac{2y\left(v_{\mathrm{ph}} \pm 1\right)}{v_{\mathrm{ph}}}, \quad y = \pi f L_a, \quad \mathrm{Ci}(x) = -\int_x^\infty dt\frac{\cos t}{t}, \quad \mathrm{Si}(x) = \int_0^x dt\frac{\sin t}{t}, \tag{2.80}$$

the auto-correlation coefficient can be expressed as:

$$\begin{aligned}\Gamma_{aa}(f) = 3v_{\mathrm{ph}}^4 - 2v_{\mathrm{ph}}^2 + \frac{v_{\mathrm{ph}}^5}{64y^3}\Big\{&24yx_+x_-\left[\mathrm{Ci}\left(x_+\right) - \mathrm{Ci}\left(x_-\right) - 2\,\mathrm{arcoth}\left(v_{\mathrm{ph}}\right)\right] \\ &+ 3x_+^2x_-^2\left[\mathrm{Si}\left(x_+\right) - \mathrm{Si}\left(x_-\right)\right] + 3\left(2 + x_+x_-\right)\left(x_-\cos x_+ - x_+\cos x_-\right) \\ &+ 6\left[1 - \left(3 + 1/v_{\mathrm{ph}}\right)yx_-\right]\sin x_+ - 6\left[1 - \left(3 - 1v_{\mathrm{ph}}\right)yx_+\right]\sin x_-\Big\}.\end{aligned} \tag{2.81}$$

It is informative to compare the GR limit of this result with the result from the Hellings & Downs correlation (Eq. (2.36)).

In the HD result, the auto-correlation coefficient is $\Gamma_{aa}^{\text{HD}} = 1$. This can be derived by looking at correlation of the Earth and pulsar term for identical pulsars $a = b$, which are expressed through the exponential factors in Eq. (2.34). The correlations are the same size for identical pulsars and the exponential terms now lead to an additional factor of two in the HD curve in Eq. (2.40), alongside the fast oscillating terms:

$$\Gamma_{ab}^{\text{HD}} = (1+\delta_{ab})\Big[\frac{3}{2}x_{ab}\ln(x_{ab}) - \frac{1}{4}x_{ab} + \frac{1}{2}\Big] \tag{2.82}$$

For two identical pulsars the angle between the pulsars is zero $\xi_{ab} = 0$ and thus $x_{ab} = 0$. With this, and the chosen normalization factors $\frac{2}{3}$ and $\frac{3}{2}$ in Eqs. (2.34) and (2.36) respectively, the result for the auto-correlation is $\Gamma_{aa}^{\text{HD}} = 1$.

The GR limit of $\Gamma_{aa}(f)$ in Eq. (2.81) is given by evaluating the integral of the modified gravity auto-correlation in Eq. (2.79) for $v_{ph} = c = 1$:

$$\Gamma_{aa}^{\text{GR}} = \frac{3}{4}\int_0^{\pi} d\theta \frac{\sin^5\theta \sin^2(\pi f L_a(1+\cos\theta))}{(1+\cos\theta)^2} = 1 - \frac{3(1-\text{sinc}(4\pi f L_a))}{8(\pi f L_a)^2}. \tag{2.83}$$

The result Γ_{aa}^{GR} depends on the frequency f and the the pulsar distance L_a. Initially this dependence may seem significant, because it obviously does not exist for the HD result, but due to the long arm limit $fL_a \gg 1$ in PTA analyses, the auto correlation coefficient in GR can be approximated to:

$$\Gamma_{aa}^{\text{GR}}(f) \overset{fL_a \gg 1}{\approx} \Gamma_{aa}^{\text{HD}}(f) = 1 \tag{2.84}$$

thus making the effect of the dependence irrelevant.

While the auto correlation coefficient in Eq. (2.81) is the main result in [12], another observation is made in the large-fL_a limit which is significant for the analysis of PTA data when considering subluminal velocities.
Expanding the result in Eq. (2.81) in order of $(fL_a)^{-1}$ leads to a linear scaling of the auto correlation coefficient Γ_{aa}:

$$\Gamma_{aa}(f) = \Gamma_{aa}^{\text{limit}} + \mathcal{O}\Big(\Big(\frac{1}{fL_a}\Big)^0\Big) = \Theta(-\log_{10} v_{ph})\frac{3\pi^2}{4} f L_a v_{ph}(v_{ph}^2 - 1)^2 + \mathcal{O}\Big(\Big(\frac{1}{fL_a}\Big)^0\Big). \tag{2.85}$$

If phase velocities equal or close to the speed of light are considered, the $(v_{ph}^2 - 1)^2$ factor in Eq. (2.85) limits Γ_{aa}. However, if the velocities are no longer in this range close to c, the auto-correlation coefficient becomes of the order of fL_a and much larger than the cross-correlations at $\xi \neq 0$. When exactly this effect occurs is be determined by solving $\Gamma_{aa}^{\text{limit}} \gtrsim 1$ for v_{ph}:

$$v_{ph} \lesssim \bar{v}_{ph} = 1 - \frac{1 + \sqrt{3\pi^2 f L_a}}{3\pi^2 f L_a}. \tag{2.86}$$

From this follows for the auto- and cross-correlation: $\Gamma_{aa} \gtrsim 1 \gtrsim \Gamma_{ab}$.
The distances of pulsars are usually of the order $fL_a \sim \mathcal{O}(100...1000)$ and when applying this to the result for v_{ph} above, it becomes clear that if the phase velocity deviates from the speed of light only by a small percentage, the difference between auto- and cross correlation coefficients increases. The auto-correlation coefficient becomes significantly larger, which can also be seen in Figure 2.5.

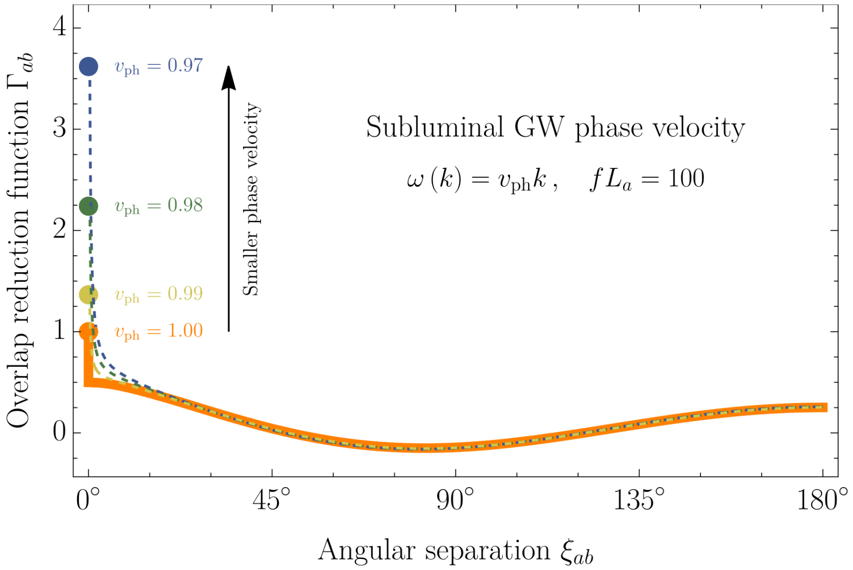

Figure 2.5: Modification of the HD curves with model of subluminal phase velocities $v_{ph} < 1$. With increasing deviation of the phase velocity from the speed of light, the discrepancy between the cross- and auto-correlation coefficient also increases, as the latter becomes much larger. [12].

For a clearer understanding of this effect, the detector pattern functions as defined in Eq. 2.33 for GR and in Eq. 2.63 for modified gravity, are studied more closely. In general relativity F_a^A becomes enhanced under the condition that the relative angle between the pulsar $\hat{\boldsymbol{p}}_{\boldsymbol{a}}$ and the propagation direction $\hat{\boldsymbol{\Omega}}$ of the gravitational wave is $\theta = \pi$. But, at this condition the integrand in the GR auto-correlation coefficient in Eq. 2.83 vanishes, so that an enhancement by the denominator is no longer possible.
In modified gravity the denominator in F_a^A becomes large if $\hat{\boldsymbol{\Omega}} \cdot \hat{\boldsymbol{p}}_{\boldsymbol{a}} = -v_{ph}$, or $\cos\theta = -v_{ph}$. In this case, the value of integrand in Eq. 2.79 increases for angles θ fulfilling this condition.

Finding that the auto-correlation coefficient is enhanced for $v_{ph} < 1$ has significant consequences for the previously introduced analysis of PTA data. For phase velocities that are considerably smaller than the bound in Eq. (2.86), the ORF can be approximated as follows:

$$v_{ph} \lesssim \bar{v}_{ph} \quad \Rightarrow \quad \Gamma^{\mathrm{SIM}}_{ab}(f) \approx \delta_{ab}\frac{3}{4}\pi^2 f L_a v_{ph}(v_{ph}^2 - 1)^2, \tag{2.87}$$

where the cross-correlations are dropped entirely.

The cross-power spectrum, also timing-residual power spectrum, S_{ab} can be defined as:

$$S_{ab} = \frac{1}{6\pi^2 f^2}\Gamma_{ab} S_h(f), \tag{2.88}$$

with the strain power spectrum $S_h(f)$ and the overlap reduction function. $S_h(f)$ in return is expressed through the characteristic strain h_c with a power law ansatz:

$$S_h = \frac{h_c^2}{2f} = \frac{A^2}{2f}\left(\frac{f}{f_{ref}}\right)^{2\alpha}. \tag{2.89}$$

With the equations above, the approximated cross-power spectrum for modified gravity is:

$$S_{ab} \approx \delta_{ab} f L_a \frac{A^2 v_{ph}(v_{ph}^2 - 1)^2}{16 f_{ref}^3}\left(\frac{f}{f_{ref}}\right)^{-(3-2\alpha)}. \tag{2.90}$$

The expression indicates that S_{ab} is proportional to $f L_a A^2 v_{ph}(v_{ph}^2 - 1)^2$. This result is studied in the PTA data analysis and further discussed in section 4.

3 Principles of PTA analysis

This chapter focuses on the analysis of PTA data and the implementation of the ORF derived from Legendre polynomials (Sec. 2.3.2), as well as the approximated ORF (Sec. 2.3.3), in order to compare them with the data. For this the program PTArcade is introduced, and a brief overview of the statistical methods used is given. Finally, the employed code is presented along with an explanation of its components.

3.1 PTArcade

Pulsar timing arrays can be evaluated using the PTArcade [21, 22] program. It uses Bayesian statistics for the analysis of new-physics models with PTA data. The data is acquired from observation and timing of 68 millisecond pulsars by the NANOGrav collaboration [6]. It can either be used to analyse stochastic or deterministic signals. In case of the former, the energy density spectrum of gravitational waves needs to be defined by the user.

The new-physics signals are characterized by model files written in Python which include the parameters and their priors, energy density spectrum and the overlap reduction function. As explained in section 2.3.3 the cross-power spectrum S_{ab} corresponds to the product of the ORF Γ_{ab} and the strain power spectrum S_h. The energy density spectrum $\Omega_{\mathrm{GW}}(f)$ can be expressed through S_h [23]:

$$\Omega_{\mathrm{GW}}(f) = \frac{4\pi^2}{3H_0^2} f^3 S_h(f) = \frac{4\pi^2}{3H_0^2} f^3 \frac{h_c^2}{2f}, \tag{3.1}$$

where H_0 is the Hubble constant. The characteristic strain h_c is once again modeled by a power law as in Eq. (2.89), with the parameters A, the amplitude of the gravitational wave and γ. From this follows the following expression for the energy density spectrum, which is implemented into PTArcade:

$$h^2\Omega_{\mathrm{GW}}(f) = \frac{2\pi^2}{3}\left(\frac{h}{H_0}\right)^2 A^2 f_{yr}^2 \left(\frac{f}{f_{yr}}\right)^{5-\gamma}. \tag{3.2}$$

In the implementation, several corrections need to be considered in the timing residuals of the pulsars and thus also in the model. This includes corrections between the frame of the pulsar system and the Solar System Barycenter (SSB) frame and between the observatory and the SSB frame. The corrections also include white noise and pulsar intrinsic red noise. To keep this section concise, a detailed discussion of these corrections is not provided here, but can be found in, among others, Mitridate et al. [22] and Taylor [1]. However, it becomes evident that these corrections lead to a large number of parameters in the model, showing the extent of the parameter space.

Before discussing the specifics of the employed code and its configuration in PTArcade, a brief introduction to Bayesian statistics and Markov Chain Monte Carlo methods is given. Together they are used for the calculation of posterior probability distributions of the relevant parameters.

3.1.1 Bayesian statistics

In Bayesian probability theory, prior knowledge about the preformed analysis is included in the model. There are essentially four parts to Bayes theorem: the prior $p(H|I)$, the likelihood function $p(D|H,I)$ and the resulting posterior probability $p(H|D,I)$, which are related by the following expression:

$$p(H|D,I) = \frac{p(H|I)\,p(D|H,I)}{p(D|I)}. \tag{3.3}$$

Here H stands for the hypothesis, D for the observed data and I represents the background information. The prior contains the knowledge that already exists about the data before actually seeing it. The likelihood function describes the probability of finding the observed data if the hypothesis is true. From this it follows that the posterior probability fully describes the extent of information known about the hypothesis [24]. The theorem can also be expressed in terms of the model M and the parameters of the model θ [25]:

$$p(\theta|D,M) = \frac{p(\theta|M)\,p(D|\theta,M)}{p(D|M)}. \tag{3.4}$$

The denominator is called the marginal likelihood or evidence, which normalizes the posterior distribution. It can be calculated for the model M with parameters θ by integrating over the product of the prior distribution and the likelihood of parameters:

$$p(D|M) = \int d\theta\; p(\theta|M)\,p(D|M,\theta). \tag{3.5}$$

It gauges how well the data D is described by the chosen model M after the average over all the parameters and is mainly used to compare models using the Bayes factor, which corresponds to the ratio of the evidences of two different models. The likelihood also serves as a normalization factor, ensuring that the posterior distribution integrates to unity over all parameters.

In PTArcade the posterior probability distributions for the model parameters are calculated. As discussed, the models for the gravitational wave signals include a large number of parameters. To obtain information about the relevant parameters, the posterior distribution needs to be integrated over all unwanted ones [26]. The large parameter space makes calculating these integrals very difficult. This problem of high dimensionality is solved by using Markov Chain Monte Carlo (MCMC) method.

3.1.2 Markov Chain Monte Carlo

This section summarizes some of the crucial aspects of MCMC, following Speagle [25], where an introduction to the method is given, focusing on a conceptual understanding. The essential aspect of MCMC is that it creates a chain of parameter values or samples over n iterations $\theta_1...\theta_n$. The density of samples $\rho(\theta)$ or, the number of iterations in a region of a certain parameter value, is then proportional to the the posterior probability distribution $p(\theta|D, M)$. When analyzing data, the discrete samples are used to estimate the integral over the posterior distribution in the considered region.

The chains are created by the Metropolis-Hastings algorithm, where new samples $\theta_i \rightarrow \theta_{i+1}$ in the chain are generated. The resulting density distributions $\rho(\theta)$ need to fulfill the following requirements:

1. $\rho(\theta)$ must converge in the limit of infinite iterations n.
2. $\rho(\theta)$ must be equal to the posterior probability distribution.

The first requirement is satisfied when employing that the probability does not change, or is conserved, when taking a step $\theta_i \rightarrow \theta_{i+1}$. This is also called detailed balance. To take such a step the algorithm first proposes a new position, and then the transition probability of the step is computed. If this transition probability is higher than a randomly generated number, the step is accepted. If it is smaller, the step is rejected and θ_{i+1} is set to θ_i. This process is then repeated until the chain converges.

From this it becomes clear, that the new position in the chain only depends on the current position. These types of chains are called Markov chains and the simulation of new positions in this way is typically used in Monte Carlo simulations. This gives light to origin of the name for MCMC. It is essentially the combination of the two methods, allowing for the probability distribution to be acquired, without encountering the problem of high dimensions.

3.2 Model File Implementation

The model file used for the analysis of the modified gravity signal can been seen below. The mode **enterprise** [27, 28] is used, as this establishes the analysis of the data on the level of timing residuals [22]. The priors for the parameters A and γ are chosen according to [6]. It is important to note that the priors for the amplitude and phase velocity are given as the logarithm of the respective value. As mentioned before, this is done in order to cover a wide range of values effectively. The prior of the phase velocity is set to a uniform distribution in the interval $[-1, 0]$ for subluminal velocities, and to $[-1, 1]$ for sub- and superluminal velocities.

The auto-correlation coefficient is defined in lines 19 to 38, starting off with establishing the value for the fixed pulsar distance. For the GR case ($v_{ph} = 1$) the coefficients output corresponds to Eq.

(2.83). For all other cases, the output consists of the term in Eq. (2.81), which has been split up into smaller terms for a clearer structure. In lines 40 to 49 the overlap reduction function is constructed, where first the numerical values acquired from the Legendre formalism in Eq. (2.58) are loaded into the file. The Python code used to compute the a_ℓ coefficients, which are essential for the numerical calculation, is included in the Appendix B. For the same pulsar positions (pos1 = pos2) the ORF returns the previously defined auto-correlation coefficient. For all other cases, the ORF corresponds to the calculated values of the Legendre decomposition with the parameters ξ and v_{ph}. Finally, the spectrum of the signal is defined according to Eq. (3.2).

For each of the two model files ($\log_{10}(v_{ph}) \in [0, 1]$ and $[-1, 1]$) three runs are performed with different values for the fixed pulsar distance seen in line 21 of the code. The $L = 100T$ corresponds to roughly 0.5 kpc. Additional runs are done with $L = 300T$ and $L = 500T$, corresponding to a distance of 1.5 kpc and 2.5 kpc respectively. This ensures that pulsars are covered across three categories: those close to the Earth, the most common distance, and those furthest away.
In addition, three runs are performed for the approximated ORF in section 2.3.3 for a subluminal velocity prior $\log_{10}(v_{ph}) \in [-1, 0]$. The ORF (line 40 to 49) is replaced by the expression in Eq. (2.87) and the expression for the auto-correlation coefficient removed. The spectrum is defined as before. The results of the runs and their interpretation are discussed in the following section.

```
1   import numpy as np
2   from scipy.special import sici
3   import pickle
4   import ptarcade.models_utils as aux
5   from ptarcade.models_utils import prior
6   from enterprise import constants as const
7
8   name = "v_neq_c2"
9
10  smbhb = False                #excluding an expected signal of super massive black hole binaries
11
12  #A and gamma priors as in [6]
13  parameters = {
14    "log10_v": prior("Uniform", -1, 0),
15    "log10_A": prior("Uniform", -18, -11),
16    "gamma": prior("Uniform", 0, 7)
17  }
18  #auto correlation coefficient
19  def auto_corr(vph, f):
20    T_obs = f[0]**(-1)         #Timing baseline in sec
21    L = 100*T_obs              #Fixed pulsar distance in sec
22    Pi = np.pi
23    y = Pi*f*L
24    x_minus = (2*y*(vph-1))/vph
25    x_plus = (2*y*(vph+1))/vph
26    if vph == 1:
27      return 1 - 3/(8 * (f*L)**2 * Pi**2) + (3 * np.sin(4 * (f*L) * Pi))/(32 * (f*L)**3 * Pi**3)
28    else:
29      term1 = 3*vph**4
30      term2 = -2*vph**2
```

```
        term3 = 24*y*x_plus*x_minus*(sici(x_plus)[1]-sici(x_minus)[1]-2*np.emath.arctanh(1/vph).real)
        term4 = 3*(x_minus)**2 * (x_plus)**2 * (sici(x_plus)[0] - sici(x_minus)[0])
        term5 = 3*(2+x_minus*x_plus)*(x_minus*np.cos(x_plus) - x_plus*np.cos(x_minus))
        term6 = 6*(1-(3+(1/vph))*y*x_minus)*np.sin(x_plus)
        term7 = -6*(1-(3-(1/vph))*y*x_plus)*np.sin(x_minus)

        result = term1 + term2 + (vph**5/(64*y**3))*(term3 + term4 + term5 + term6 + term7)
        return result

with open('ORF_func.pkl', 'rb') as f:        #numerical values of the ORF from the Legendre decomposition
    ORF_func = pickle.load(f)

#overlap reduction function
def orf(f, pos1, pos2, log10_v, log10_A, gamma):
    if np.all(pos1 == pos2):
        return auto_corr(vph = 10**log10_v, f = f)
    else:
        xi = np.arccos(np.dot(pos1, pos2))
        return ORF_func(log10_v, xi)

# spectrum
def spectrum(f, log10_v, log10_A, gamma):

    return 2*np.pi**2/3 * (aux.h/aux.H_0)**2 * (10 ** log10_A)** 2 * const.fyr**2 * (f/const.fyr)**(5 - gamma)
```

4 Results

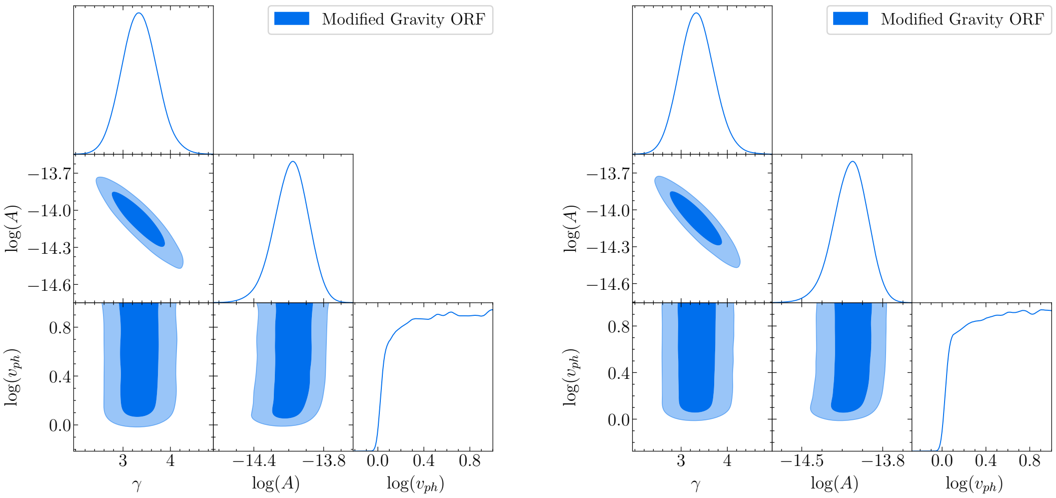

(**a**) Sub − & Superluminal phase velocities, $L = 100T$

(**b**) Sub − & Superluminal phase velocities, $L = 300T$

(**c**) Sub − & Superluminal phase velocities, $L = 500T$

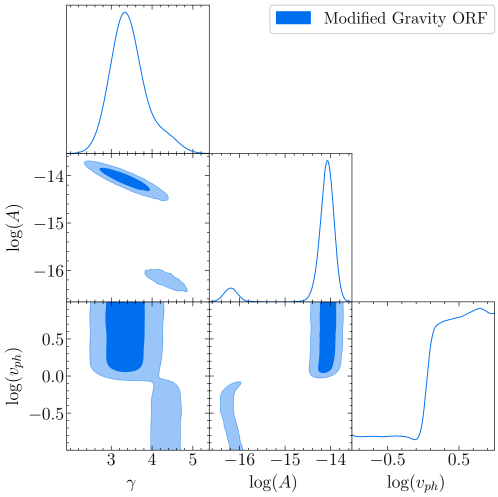

Figure 4.1: Posterior distribution for the model with the modified gravity ORF $\Gamma_{ab}^{\mathrm{LD}}$ from Eq. (2.78), with the phase velocity prior $\log_{10}(v_{ph}) \in [-1, 1]$. The energy density spectrum is defined as in Eq. (3.2) and the three plots each correspond to a different fixed pulsar distance: $L = 100T$ (a), $L = 300T$ (b), and $L = 500T$ (c).

Figure 4.1 shows the corner plots resulting from the runs for sub- and superluminal phase velocities for fixed pulsar distances: $L = 100T$ (a), $L = 300T$ (b), and $L = 500T$ (c). The posterior distribution function for the logarithm of the phase velocity shows that the superluminal phase velocities $\log_{10}(v_{ph}) > 0$ ($v_{ph} < 1$ and the GR case at $\log_{10}(v_{ph}) = 0$ ($v_{ph} = 1$) are preferred over the subluminal phase velocities $\log_{10}(v_{ph}) < 0$ ($v_{ph} < 1$). This trend can be seen in all three plots, implying that the superluminal phase velocities are better in agreement with the NANOGrav PTA data than the subluminal. However, for the linear dispersion relation considered in this work (Eq. 2.41) and discussed in Sec. 2.3, phase velocities larger than one lead to violation of causality.

While examining the data for $v_{ph} > 1$ is of interest, it does not give any physically reasonable results.

Figure 4.2 shows the corner plots resulting from the implementation of the modified gravity ORF Γ_{ab}^{LD} and the simplified ORF Γ_{ab}^{SIM}. As stated in the previous section, a subluminal phase velocity prior was chosen $\log_{10}(v_{ph}) \in [-1, 0]$. The three plots (a), (b) and (c) each correspond respectively to the different fixed pulsar distances $L = 100T, 300T, 500T$.

The key observation is found in the two dimensional posterior distribution of $\log_{10}(A)$ and $\log_{10}(v_{ph})$. For small phase velocities $v_{ph} \ll 1$, the posterior distribution corresponding to the simplified Γ_{ab}^{SIM} closely matches the results from modified gravity. For phase velocities close to the speed of light however, the two models show less agreement, due to the fact that the simplified ORF is valid only for the bound specified in Eq. (2.86).

In addition, for phase velocities $v_{ph} < c$ a flat direction in the parameter space of the amplitude and phase velocity can be observed in each of the three plots. This indicates a parameter degeneracy in A and v_{ph}, meaning that the posterior distribution takes on similar or identical values over different combinations of the parameters. To emphasize this the parameter combination that the posterior distribution is sensitive for is studied:

$$P_X = fLA^2 v_{ph}(v_{ph}^2 - 1)^2. \tag{4.1}$$

P_X is calculated for the maximum value of A, $v_{ph} = 0.1$, the fixed pulsar distance L and the frequency $f_1 = \frac{1}{T}$. The maximum values of the amplitude are determined using a kernel density estimation (KDE) with gaussian_kde [29] and listed in Table 4.1. These values for P_X and A_{max} are calculated for both the modified gravity and the simplified ORF, considering each of the fixed pulsar distances. Using the computed values of P_X, a curve running along the maximum of the two-dimensional posterior distribution of each Γ_{ab}^{LD} and Γ_{ab}^{SIM} is added to the respective plots.
Looking first at maximum values of the amplitude, it becomes clear that $\log_{10}(A_{\text{max}})$ decreases as the fixed pulsar distance increases. This is consistent with the expectation that the amplitude of the gravitational wave signal declines with greater pulsar distances. The values of $\log_{10}(A_{\text{max}})$ for the simplified ORF deviate from the values of the modified gravity ORF by less than 0.26%. This highlights once again, that Γ_{ab}^{SIM} is an excellent approximation for phase velocities $v_{ph} \ll 1$.

(**a**) Subluminal phase velocities, $L = 100T$

(**b**) Subluminal phase velocities, $L = 300T$

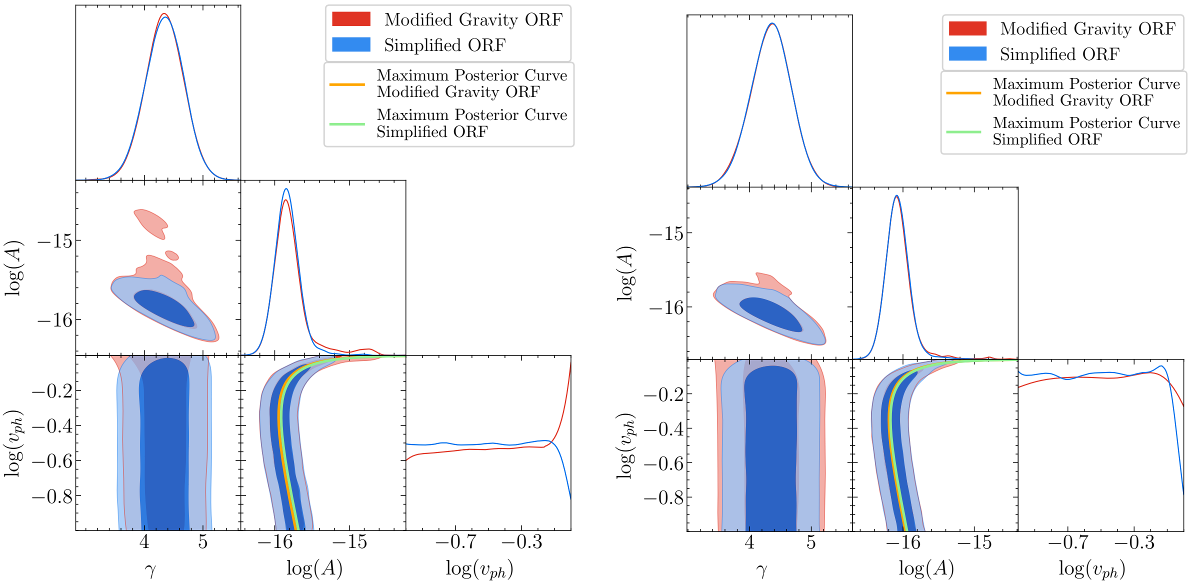

(**c**) Subluminal phase velocities, $L = 500T$

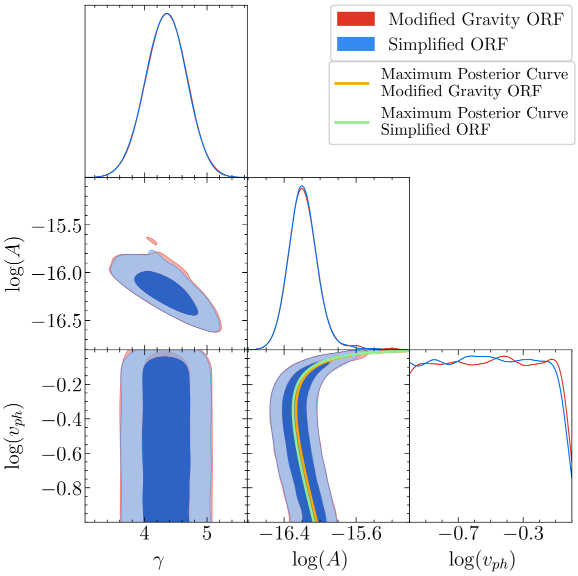

Figure 4.2: Posterior distributions resulting from the model files of the modified gravity ORF $\Gamma_{ab}^{\mathrm{LD}}$ in Eq. (2.78) and the simplified ORF $\Gamma_{ab}^{\mathrm{SIM}}$ in Eq. (2.87). The prior for the phase velocity is $\log_{10}(v_{ph}) \in [-1, 0]$ and the energy density spectrum is defined as in Eq. (3.2). The plots correspond to the values implemented for the fixed pulsar distance: $L = 100T$ (a), $L = 300T$ (b) and $L = 500T$ (c). In the posterior distribution for $\log_{10}(v_{ph})$ and $\log_{10}(A)$ (**lower middle**) a degeneracy in the parameter space can be identified. Two curves are plotted along the maximum of the posterior distribution according to Eq. (4.1), each with the respective values of A_{max} for both models (see Table 4.1).

	$\log(A_{\text{max}})$ for Γ_{ab}^{LD}	$\log_{10}(A_{\text{max}})$ for Γ_{ab}^{SIM}	P_X for Γ_{ab}^{LD}	P_X for Γ_{ab}^{SIM}
L = 100T	-15.72	-15.68	3.62 E-31	4.26 E-31
L = 300T	-15.97	-15.94	3.45 E-31	3.83 E-31
L = 500T	-16.04	-16.07	4.17 E-31	3.57 E-31

Table 4.1: Maximum values of the logarithmic amplitude $\log(A_{\text{max}})$ and P_X as defined in Eq. (4.1). The values are determined for both the modified gravity ORF Γ_{ab}^{LD} and simplified ORF Γ_{ab}^{SIM} and for the three fixed pulsar distances, corresponding to 0.5 kpc, 1.5 kpc and 2.5 kpc respectively.

The resulting values of P_X are also presented in 4.1 and are found to all roughly equal 4×10^{-31}. The newly identified flat direction in the parameter space can thus be roughly summarized by this constraint:

$$f_1 L A^2 v_{ph} (v_{ph}^2 - 1)^2 \sim 4 \times 10^{-31}. \tag{4.2}$$

This parameter combination coincides with the proportionality of the cross power spectrum found in Sec. 2.3.3, Eq. (2.90):

$$S_{ab} \propto f_1 L A^2 v_{ph} (v_{ph}^2 - 1)^2. \tag{4.3}$$

Based on this result, it can be concluded that the combinations of these parameters: v_{ph}, A and L_a that satisfy the constraint $S_{ab} \sim 4 \times 10^{-31}$, are favoured by the PTA data.

5 Conclusion and outlook

Pulsar timing arrays (PTAs) have proven to be a powerful tool for the detection and study of gravitational waves, providing important insight to not only classical but also modified gravity theories. In this thesis, the Hellings and Downs (HD) curve, which is the overlap reduction function (ORF) describing a characteristic correlation pattern in general relativity, was studied through two previously established derivations. The analytical approach provided a fundamental understanding of the HD curve within the context of general relativity. The decomposition into spherical harmonics presented an alternative method frequently utilized in cosmic microwave background studies.

The result of the spherical harmonical decomposition was then used to analyze the correction to the HD curve in modified gravity theories, particularly for subluminal phase velocities. Significant findings regarding the auto-correlation coefficient Γ_{aa} were drawn from recent research, demonstrating that Γ_{aa} does not diverge in case of modified gravity. Instead, an analytical expression can be found.

A simplified ORF, $\Gamma_{ab}^{\mathrm{SIM}}$, was derived for the long arm-limit, resulting in the cross power spectrum to be proportional to $fL_aA^2v_{ph}(v_{ph}^2-1)^2$. This approximation is a result of the linear dependence of Γ_{aa} on the fixed pulsar distance fL_a and of the fact that Γ_{aa} becomes significantly larger than the cross-correlation for slight deviations from general relativity.

Modified gravity models for uniform logarithmic velocity priors $\log_{10}(v_{ph}) \in [-1, 1]$ and $\log_{10}(v_{ph}) \in [-1, 0]$ were analyzed. The analysis was conducted using the program PTArcade, which utilized the developed code and the 15-year NANOGrav data set. The results of the prior range $\log_{10}(v_{ph}) \in [-1, -1]$ confirm that the data supports the GR case. The plots also indicate a better fit of the data for phase velocities $v_{ph} \geq 1$ compared to $v_{ph} \leq 1$, however this does not yield any reasonable results, as phase velocities $v_{ph} \geq 1$ lead to a violation of causality.

Key results were obtained for the subluminal phase velocity prior $\log_{10}(v_{ph}) \in [-1, 0]$. The two sets of posteriors, corresponding to the modified gravity ORF $\Gamma_{ab}^{\mathrm{LD}}$ and the simplified ORF $\Gamma_{ab}^{\mathrm{SIM}}$, show almost identical distributions for $v_{ph} \ll 1$.

A degeneracy in parameter space of $\log_{10}(v_{ph})$ and $\log_{10}(A)$ is evident. The values of the parameter combination $P_X = fLA^2v_{ph}(v_{ph}^2-1)^2$, which the posterior distribution is sensitive to, are calculated for A_{max}, $v_{ph} = 0.1$ and the respective pulsar distances L. Following from these values, an additional curve is plotted long the maximum posterior density. A comparison of the value for $\log_{10}(A_{\mathrm{max}})$ for $\Gamma_{ab}^{\mathrm{LD}}$ and $\Gamma_{ab}^{\mathrm{SIM}}$ highlights, that the simplified ORF is a fitting approximation for sufficiently small phase velocities.

The resulting expression of P_X corresponds to the proportionality of the cross-power spectrum S_{ab} found in Eq. 2.90. The values P_X are found to roughly correspond to the value of 4×10^{-31}. Due the correlation between P_X and the proportionality found for S_{ab}, this roughly constrains the cross power spectrum to this factor: $S_{ab} \sim 4 \times 10^{-31}$.

The analysis presented in this thesis allows future research to further examine the implications of modified gravity theories in PTA data, using the derived auto-correlation coefficient i.e. the simplified overlap reduction function. This simplified ORF and the constraints on the cross-power spectrum S_{ab} can be integrated into upcoming studies with different or more refined datasets. This could potentially allow for the detection of deviations from general relativity that may have previously gone unnoticed. Future work could, for example, include the integration of more precise pulsar distances, allowing for a more refining analysis regarding the effect of fL on the constraint of S_{ab}.

Appendix

The Python code used for the calculating the a_ℓ coefficients can be seen below. The definition of the integral in lines 8 to 20 is constructed as in eq. (2.69) and the values for the phase velocity are defined logarithmically. Finally, a loop (line 38 to 52) over v_{ph} and ℓ first calculates the c_ℓ, and then the a_ℓ coefficients for $\ell = 2$ to $\ell = 20$. The parameters fL specify the fixed pulsar distance.

```
 1  # Parameters  fL=100
 2  f = 10
 3  L = 10
 4
 5  x = symbols('x')
 6
 7  # Compute the integrand
 8  def create_integrand(ell, v_ph):
 9      # Legendre polynomial and second derivative
10      P_l = legendre(ell, x)
11      P_l_double_prime = diff(P_l, x, x)
12      # For numerical evaluation
13      P_l_double_prime_func = lambdify(x, P_l_double_prime, 'numpy')
14      # 3 terms of the integral
15      def integrand(x):
16          term1 = (1 - x**2)**2 / (1 + x / v_ph)
17          term2 = 1 - np.exp(-1j * 2 * np.pi * f * L * (1 + (x / v_ph)))
18          term3 = P_l_double_prime_func(x)
19          return term1 * term2 * term3
20      return integrand
21
22  # Integration limits
23  a, b = -1, 1
24  # Limit of subdivisions
25  limit_subdivisions = 10000
26
27  # v_ph logarithmically spaced values from 0.1 to 10
28  logv_values = [
29      -1.00, -0.95, -0.90, -0.85, -0.80, -0.75, -0.70, -0.65, -0.60, -0.55,
30      -0.50, -0.45, -0.40, -0.35, -0.30, -0.25, -0.20, -0.15, -0.10, -0.05,
31       0.00,  0.05,  0.10,  0.15,  0.20,  0.25,  0.30,  0.35,  0.40,  0.45,
32       0.50,  0.55,  0.60,  0.65,  0.70,  0.75,  0.80,  0.85,  0.90,  0.95,
33       1.00
34  ]
35  v_ph_values = [10 ** x for x in logv_values]  # v_ph values
36
37  # Loop over v_ph and ell
38  a_ell_results = {}
39  for logv, v_ph in zip(logv_values, v_ph_values):
40      for ell in range(2, 21):  # From 2 to 20
41          integrand = create_integrand(ell, v_ph)
42          # Real part
43          result_real, error_real = quad(lambda x: np.real(integrand(x)), a, b, limit=limit_subdivisions)
44          # Imaginary part
45          result_imag, error_imag = quad(lambda x: np.imag(integrand(x)), a, b, limit=limit_subdivisions)
46          # Absolute value
47          c_ell = np.abs(result_real + 1j * result_imag)
48          # Calculate a_ell
49          a_ell = (3/2) * (2*ell + 1) * math.factorial(ell - 2) / math.factorial(ell + 2) * (c_ell**2) / 16
50          if ell not in a_ell_results:
51              a_ell_results[ell] = []
52          a_ell_results[ell].append((logv, a_ell))
53
```

Bibliography

[1] Stephen R. Taylor. *The Nanohertz Gravitational Wave Astronomer*. 2021. arXiv: 2105.13270 [astro-ph.HE]. URL: https://arxiv.org/abs/2105.13270.

[2] R. W. Hellings and G. S. Downs. "Upper limits on the isotropic gravitational radiation background from pulsar timing analysis." In: 265 (Feb. 1983), pp. L39–L42. DOI: 10.1086/183954.

[3] Heng Xu et al. "Searching for the Nano-Hertz Stochastic Gravitational Wave Background with the Chinese Pulsar Timing Array Data Release I". In: *Research in Astronomy and Astrophysics* 23.7 (June 2023), p. 075024. ISSN: 1674-4527. DOI: 10.1088/1674-4527/acdfa5. URL: http://dx.doi.org/10.1088/1674-4527/acdfa5.

[4] J. Antoniadis et al. "The second data release from the European Pulsar Timing Array: III. Search for gravitational wave signals". In: *Astronomy amp; Astrophysics* 678 (Oct. 2023), A50. ISSN: 1432-0746. DOI: 10.1051/0004-6361/202346844. URL: http://dx.doi.org/10.1051/0004-6361/202346844.

[5] Daniel J. Reardon et al. "Search for an Isotropic Gravitational-wave Background with the Parkes Pulsar Timing Array". In: *The Astrophysical Journal Letters* 951.1 (June 2023), p. L6. ISSN: 2041-8213. DOI: 10.3847/2041-8213/acdd02. URL: http://dx.doi.org/10.3847/2041-8213/acdd02.

[6] Gabriella Agazie et al. "The NANOGrav 15 yr Data Set: Evidence for a Gravitational-wave Background". In: *The Astrophysical Journal Letters* 951.1 (June 2023), p. L8. ISSN: 2041-8213. DOI: 10.3847/2041-8213/acdac6. URL: http://dx.doi.org/10.3847/2041-8213/acdac6.

[7] Michele Maggiore. *Gravitational Waves. Vol. 2: Astrophysics and Cosmology*. Oxford University Press, Mar. 2018. ISBN: 978-0-19-857089-9.

[8] Jonathan Gair et al. "Mapping gravitational-wave backgrounds using methods from CMB analysis: Application to pulsar timing arrays". In: *Physical Review D* 90.8 (Oct. 2014). ISSN: 1550-2368. DOI: 10.1103/physrevd.90.082001. URL: http://dx.doi.org/10.1103/PhysRevD.90.082001.

[9] Yan-Chen Bi et al. *Constraints on the velocity of gravitational waves from NANOGrav 15-year data set*. 2023. arXiv: 2310.08366 [astro-ph.CO]. URL: https://arxiv.org/abs/2310.08366.

[10] Qiuyue Liang, Meng-Xiang Lin, and Mark Trodden. *A Test of Gravity with Pulsar Timing Arrays*. 2023. arXiv: 2304.02640 [astro-ph.CO]. URL: https://arxiv.org/abs/2304.02640.

[11] Qiuyue Liang, Ippei Obata, and Misao Sasaki. *Testing Gravity with Frequency-Dependent Overlap Reduction Function in Pulsar Timing Array*. 2024. arXiv: 2405.11755 [astro-ph.CO]. URL: https://arxiv.org/abs/2405.11755.

[12] Nina Cordes et al. *On the overlap reduction function of pulsar timing array searches for gravitational waves in modified gravity*. 2024. arXiv: 2407.04464 [gr-qc]. URL: https://arxiv.org/abs/2407.04464.

[13] Sean Carroll. *Spacetime and Geometry: An Introduction to General Relativity*. Benjamin Cummings, 2003. ISBN: 0805387323. URL: http://www.amazon.com/Spacetime-Geometry-Introduction-General-Relativity/dp/0805387323.

[14] Nigel T. Bishop and Luciano Rezzolla. "Extraction of gravitational waves in numerical relativity". In: *Living Reviews in Relativity* 19.1 (Oct. 2016). ISSN: 1433-8351. DOI: 10.1007/s41114-016-0001-9. URL: http://dx.doi.org/10.1007/s41114-016-0001-9.

[15] Michele Maggiore. *Gravitational Waves. Vol. 1: Theory and Experiments*. Oxford University Press, 2007. ISBN: 978-0-19-171766-6, 978-0-19-852074-0. DOI: 10.1093/acprof:oso/9780198570745.001.0001.

[16] Melissa Anholm et al. "Optimal strategies for gravitational wave stochastic background searches in pulsar timing data". In: *Physical Review D* 79.8 (Apr. 2009). ISSN: 1550-2368. DOI: 10.1103/physrevd.79.084030. URL: http://dx.doi.org/10.1103/PhysRevD.79.084030.

[17] Fredrick A. Jenet and Joseph D. Romano. *Understanding the gravitational-wave Hellings and Downs curve for pulsar timing arrays in terms of sound and electromagnetic waves*. 2015. arXiv: 1412.1142 [gr-qc]. URL: https://arxiv.org/abs/1412.1142.

[18] Glauber Carvalho Dorsch and Lucas Emanuel Antunes Porto. “An introduction to gravitational waves through electrodynamics: a quadrupole comparison”. In: *European Journal of Physics* 43.2 (Jan. 2022), p. 025602. ISSN: 1361-6404. DOI: 10.1088/1361-6404/ac4645. URL: http://dx.doi.org/10.1088/1361-6404/ac4645.

[19] Marc Kamionkowski, Arthur Kosowsky, and Albert Stebbins. “A Probe of Primordial Gravity Waves and Vorticity”. In: *Physical Review Letters* 78.11 (Mar. 1997), pp. 2058–2061. ISSN: 1079-7114. DOI: 10.1103/physrevlett.78.2058. URL: http://dx.doi.org/10.1103/PhysRevLett.78.2058.

[20] John David Jackson. *Classical Electrodynamics, 3rd Edition*. Wiley & Sons Ltd, 1998. ISBN: 978-1-119-77076-3.

[21] Andrea Mitridate. *PTArcade*. Apr. 2023. DOI: 10.5281/zenodo.7876430.

[22] Andrea Mitridate et al. *PTArcade*. 2023. arXiv: 2306.16377 [hep-ph]. URL: https://arxiv.org/abs/2306.16377.

[23] Gabriella Agazie et al. *The NANOGrav 15 yr Data Set: Running of the Spectral Index*. 2024. arXiv: 2408.10166 [astro-ph.HE]. URL: https://arxiv.org/abs/2408.10166.

[24] Udo von Toussaint. “Bayesian inference in physics”. In: *Rev. Mod. Phys.* 83 (3 Sept. 2011), pp. 943–999. DOI: 10.1103/RevModPhys.83.943. URL: https://link.aps.org/doi/10.1103/RevModPhys.83.943.

[25] Joshua S. Speagle. *A Conceptual Introduction to Markov Chain Monte Carlo Methods*. 2020. arXiv: 1909.12313 [stat.OT]. URL: https://arxiv.org/abs/1909.12313.

[26] Rutger Van Haasteren et al. “On measuring the gravitational-wave background using Pulsar Timing Arrays”. In: *Monthly Notices of the Royal Astronomical Society* 395.2 (Apr. 2009), pp. 1005–1014. ISSN: 0035-8711. DOI: 10.1111/j.1365-2966.2009.14590.x. URL: https://doi.org/10.1111/j.1365-2966.2009.14590.x.

[27] Justin A. Ellis et al. *ENTERPRISE: Enhanced Numerical Toolbox Enabling a Robust PulsaR Inference SuitE*. Zenodo. Sept. 2020. DOI: 10.5281/zenodo.4059815. URL: https://doi.org/10.5281/zenodo.4059815.

[28] Stephen R. Taylor et al. *enterprise_extensions*. v2.3.3. 2021. URL: https://github.com/nanograv/enterprise_extensions.

[29] SciPy Developers. *SciPy Documentation - gaussian_kde*. https://docs.scipy.org/doc/scipy/reference/generated/scipy.stats.gaussian_kde.html. Accessed: 2024-08-25. 2024.